NASA/TM—2009-215608

SHJAR Jet Noise Data and Power Spectral Laws

Abbas Khavaran
ASRC Aerospace Corporation, Cleveland, Ohio

James Bridges
Glenn Research Center, Cleveland, Ohio

March 2009

NASA STI Program . . . in Profile

Since its founding, NASA has been dedicated to the advancement of aeronautics and space science. The NASA Scientific and Technical Information (STI) program plays a key part in helping NASA maintain this important role.

The NASA STI Program operates under the auspices of the Agency Chief Information Officer. It collects, organizes, provides for archiving, and disseminates NASA's STI. The NASA STI program provides access to the NASA Aeronautics and Space Database and its public interface, the NASA Technical Reports Server, thus providing one of the largest collections of aeronautical and space science STI in the world. Results are published in both non-NASA channels and by NASA in the NASA STI Report Series, which includes the following report types:

- TECHNICAL PUBLICATION. Reports of completed research or a major significant phase of research that present the results of NASA programs and include extensive data or theoretical analysis. Includes compilations of significant scientific and technical data and information deemed to be of continuing reference value. NASA counterpart of peer-reviewed formal professional papers but has less stringent limitations on manuscript length and extent of graphic presentations.

- TECHNICAL MEMORANDUM. Scientific and technical findings that are preliminary or of specialized interest, e.g., quick release reports, working papers, and bibliographies that contain minimal annotation. Does not contain extensive analysis.

- CONTRACTOR REPORT. Scientific and technical findings by NASA-sponsored contractors and grantees.

- CONFERENCE PUBLICATION. Collected papers from scientific and technical conferences, symposia, seminars, or other meetings sponsored or cosponsored by NASA.

- SPECIAL PUBLICATION. Scientific, technical, or historical information from NASA programs, projects, and missions, often concerned with subjects having substantial public interest.

- TECHNICAL TRANSLATION. English-language translations of foreign scientific and technical material pertinent to NASA's mission.

Specialized services also include creating custom thesauri, building customized databases, organizing and publishing research results.

For more information about the NASA STI program, see the following:

- Access the NASA STI program home page at *http://www.sti.nasa.gov*

- E-mail your question via the Internet to *help@sti.nasa.gov*

- Fax your question to the NASA STI Help Desk at 301–621–0134

- Telephone the NASA STI Help Desk at 301–621–0390

- Write to:
  NASA Center for AeroSpace Information (CASI)
  7115 Standard Drive
  Hanover, MD 21076–1320

NASA/TM—2009-215608

SHJAR Jet Noise Data and Power Spectral Laws

Abbas Khavaran
ASRC Aerospace Corporation, Cleveland, Ohio

James Bridges
Glenn Research Center, Cleveland, Ohio

National Aeronautics and
Space Administration

Glenn Research Center
Cleveland, Ohio 44135

March 2009

Acknowledgments

Support from the Subsonic Fixed Wing and Supersonic Projects under the Fundamental Aeronautics Program is greatly appreciated. The authors also acknowledge Dr. Milo Dahl, Acoustics Branch, Glenn Research Center, for his thorough and constructive comments in reviewing this report.

This report is a formal draft or working paper, intended to solicit comments and ideas from a technical peer group.

This work was sponsored by the Fundamental Aeronautics Program at the NASA Glenn Research Center.

Level of Review: This material has been technically reviewed by technical management.

Available from

NASA Center for Aerospace Information
7115 Standard Drive
Hanover, MD 21076–1320

National Technical Information Service
5285 Port Royal Road
Springfield, VA 22161

Available electronically at http://gltrs.grc.nasa.gov

Contents

List of Tables

List of Figures

SHJAR Jet Noise Data and Power Spectral Laws

Abbas Khavaran
ASRC Aerospace Corporation
Cleveland, Ohio 44135

James Bridges
National Aeronautics and Space Administration
Glenn Research Center
Cleveland, Ohio 44135

Abstract

High quality jet noise spectral data measured at the Aeroacoustic Propulsion Laboratory at the NASA Glenn Research Center is used to examine a number of jet noise scaling laws. Configurations considered in the present study consist of convergent and convergent-divergent axisymmetric nozzles. The measured spectral data are shown in narrow band and cover 8193 equally spaced points in a typical Strouhal number range of 0.0–10.0. The measured data are reported as lossless (i.e. atmospheric attenuation is added to measurements), and at 24 equally spaced angles (50^o to 165^o) on a 100-diameter (200-inches) arc.

Following the work of Viswanathan, velocity power factors are evaluated using a least squares fit on spectral power density as a function of jet temperature and observer angle. The goodness of the fit and the confidence margins for the two regression parameters are studied at each angle, and alternative relationships are proposed to improve the spectral collapse when certain conditions are met. As an immediate application of the velocity power laws, spectral density in shock-containing jets are decomposed into components attributed to jet mixing noise and shock noise. From this analysis, jet noise prediction tools can be developed with different spectral components derived from different physics.

Nomenclature

A	Jet area
B	Intercept parameter
c	Sound speed
D	Jet exit diameter (ft)
f	Frequency (Hz)
U_j	Ideally expanded jet speed (fps)
$M=U/c$	Aerodynamic Mach number
$M_j=U_j/c_j$	Ideally expanded Mach number
$M_a=U/c_\infty$	Acoustic Mach number
n	Velocity power factor
$St=f\,D/U_j$	Strouhal number based on ideally expanded jet velocity
$He=f\,D/c_\infty$	Helmholtz number
$\overline{p^2}$	Pressure spectral density (pressure^2 $\times$ sec) (i.e. Fourier transform of pressure autocorrelation function)
p_{ref}	Reference acoustic pressure
$PSD = 10Log\left(\overline{p^2}U_j/p_{ref}^2 D\right)$	Spectral density per Strouhal number, dB.

$\mathrm{Re}=U_j D/\nu$	Jet Reynolds number
T	Temperature ratio (jet temperature normalized wrt ambient temperature)
θ	Polar angle from jet inlet
ν	Kinematic viscosity
χ	Goodness factor

Subscripts:

d	Design point
e	Nozzle exit
j	Fully expanded condition
s	Static condition
t	Total or stagnation point
∞	Ambient conditions

1.1 Introduction

Development of a successful noise prediction model relies heavily on quality data. A typical narrow-band spectrum in jet noise could consist of three distinct components; the jet mixing noise, shock-associated noise and screech. As the jet exit velocity becomes supersonic (relative to the ambient conditions), the mixing noise could be complemented by an additional component at aft angles that is caused by the instabilities of the mean flow. From a modeling standpoint, it is extremely helpful if one succeeds in dividing the spectrum into components that are attributed to various generation mechanisms.

The usual procedure is to start with a jet operating condition subject to a single generation mechanism. If one can propose scaling laws for this particular noise component, then it might be possible, with various degrees of success, to subtract that from a multi-component spectrum. For example, shock-associated noise is obtained when we subtract the mixing noise from the total noise. Measurements are normally displayed as the power spectral density (PSD) per normalized frequency parameter. When multiple sources are present, they are usually regarded as completely incoherent, and in the acoustic far field, the PSD of the sum is related to the components as $10^{PSD/10} = 10^{PSD_1/10} + 10^{PSD_2/10}$.

In aeroacoustics, the most quoted scaling law is the U^8 power law derived from Lighthill's acoustic analogy [Ref. 1], as described in great detail in [Ref. 2]. It concludes that the acoustic power emitted over the surface of a large sphere surrounding a jet is proportional to the eight-power of the jet exit velocity. Other attempts to fine-tune the power law [Refs. 3, 4] consider the integrated power spectral density (i.e. the overall sound pressure level OASPL at each angle) to depend on both angle and jet temperature. Following the work of Viswanathan [Ref. 3], velocity power factors are evaluated from the narrow-band data gathered at the Small Hot Jet Acoustic Rig (SHJAR) at the NASA Glenn Research Center, applying a least squares fit on the OASPL as a function of jet temperature and observer angle. The goodness of the fit is studied at each angle, and alternative relationships are proposed that improve the spectral collapse when certain conditions are met.

Since we use the integrated spectrum as the dependent variable in a linear regression, the PSD curve scales successfully from one jet to another only when: 1) the basic shape of the spectrum is preserved; 2) the normalized frequency parameter meets the shift requirements. It will be noted that these two conditions are not always met at aft angles. However, it is possible to select a new normalized frequency parameter and collapse a major segment of the scaled spectra as long as the acoustic Mach number remains subsonic.

Supersonic jets at imperfectly expanded conditions emit broadband shock-associated noise in addition to the jet mixing noise. In many cases, shock noise is accompanied with screech. Under some conditions (unheated jets in particular) the screech tones can be very strong and result in broadband noise amplification. This amounts to an additional 3–5 dB noise enhancement throughout the spectrum. Excitation of a jet by a pure tone has been established experimentally and there are indications that this amplification happens at sideline as well as at aft angles [Refs. 5-7]. It is shown that scaling laws help identify the amplification. Since this additional noise component is a by-product of the screech, which in turn is associated with shock noise, we consider any additional amplification of the mixing noise as part of the shock noise rather than a separate entity. This assumption is instrumental if one attempts to extend the scaling laws to shock noise power intensity.

The report is organized in the following order. Section 1.2 briefly describes the SHJAR experimental setup. In section 1.3 we apply the linear least squares regression to find the velocity power factors for the jet mixing noise. The goodness of the fit, the joint confidence region of the two regression parameters, and their marginal inference interval is discussed at selective angles. Section 2 applies the scaling laws to group of convergent and convergent-divergent nozzles at various operating conditions and evaluates the quality of the spectral collapse at different angles and Mach numbers. The utility of the scaling laws are shown in section 3 when we examine various noise components. In particular, the scaling laws are employed to separate the broadband shock-associated noise from the mixing noise when supersonic jets are operating at off design conditions. In addition, it is shown that when the acoustic Mach number exceeds 1.0 the aft-angles mixing noise may be divided into two components; where one component is obtained from velocity scaling of the subsonic spectra.

1.2 Experimental Setup

Hot and cold jet noise spectral data have been acquired within the Small Hot Jet Acoustic Rig for an extensive test matrix. The SHJAR is a single stream hot jet rig located within the AeroAcoustic Propulsion Laboratory (AAPL) at the NASA Glenn Research Center. It uses remotely located compressors and a hydrogen burning combustor to provide heated air to test-nozzles at temperatures up to 1300º F and at pressures up to 150 psi. Additional noise generated by flow through piping and control valves is removed using a baffled muffler, and the flow is conditioned using screens to create clean and quiet conditions at the nozzle exit. Acoustic data repeatability has been determined to be within 0.50 dB in one-third octave bands at all frequencies [Ref. 8-11].

The AAPL, which houses the SHJAR, is a 65-foot geodesic dome lined with 24-inch long sound absorbing wedges which remove sound reflection at all frequencies above 200-Hz and provide the anechoic environment required for noise studies. The floor and all surfaces around SHJAR are covered with fiberglass wedges (Fig. 1.1). The jet exhaust from SHJAR is directed outside through a large door. Additional details about the facility are provided in references [Ref. 8,9].

For most testing, SHJAR uses a 2.0-inch nozzle, but can also operate larger nozzles with some limitation on cold set points at high Mach number. In typical testing, the SHJAR can cover a range of Mach numbers up to Mach 2.0, and static temperature ratios up to 2.8 using a hydrogen combustor and central air compressor facilities. Stagnation flow conditions for the rig are measured within a 24-inch plenum upstream of the nozzle.

Nozzles used in the present noise measurements all have a 2.0-inch exit diameter, and are designated as smcxxx, where “xxx” is a three-digits number that identifies a particular nozzle (Table 1.1). The smc000 is a baseline convergent nozzle with a 5° conic contraction and a 0.04-inch thick lip (Fig. 1.2). Convergent nozzle smc021 is a modified smc000 with the outside exit diameter filed down to a sharp edge, and fine notches (approximately 0.06-inch wide by 0.0-inch deep) cut into the edge (Fig. 1.3). The notches are 0.2-inch apart and spaced all around the nozzle lip in order to minimize the screech noise observed in the base nozzle smc000. The four CD nozzles have equal throat area and are operated at the

design pressure ratio NPR_d. In addition to the data repeatability, SHJAR measurements have also been examined vs. other existing measurements [Ref. 3, 12-16] in order to identify possible extraneous sources that are unrelated to jet noise.

Measurements are based on a test matrix designed to isolate various parameters that are thought to drive the physics of noise generation and its propagation such as constant jet velocity and constant temperature (static or stagnation). For jets operating at a pressure ratio larger than 1.89, i.e. ideal Mach number greater than 1.0, convergent-divergent nozzles were designed for ideal expansion and were tested at different temperatures. The result is a matrix of data at fixed acoustic Mach number M_a, aerodynamic Mach number M and temperature ratio T_s or T_t (static or stagnation) for a broad range of conditions, with and without screech and broadband shock-associated noise.

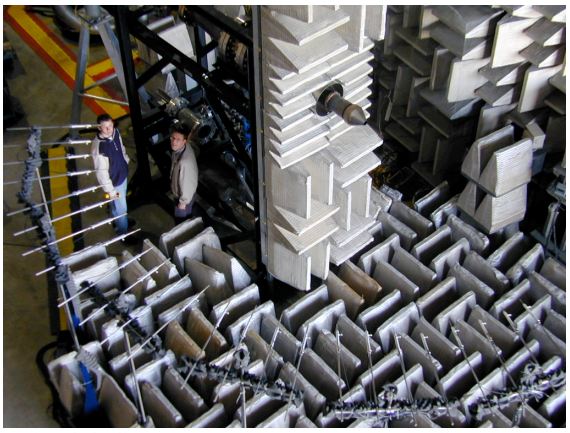

Fig. 1.1 Small Hot Jet Acoustic Rig (SHJAR)

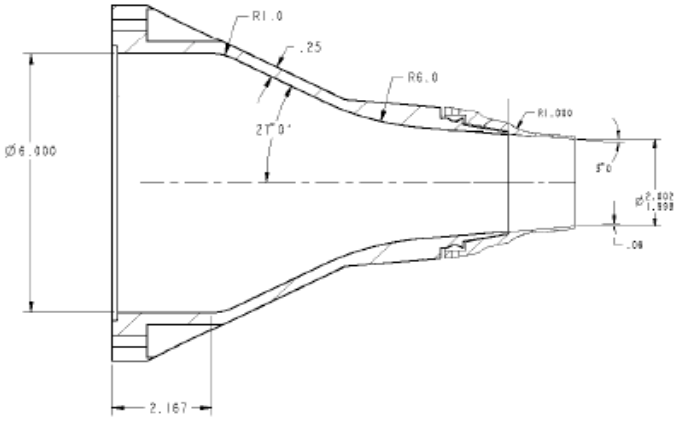

Fig. 1.2 Convergent nozzle smc000

Table 1. 1 Nozzle configurations tested in SHJAR facility

Nozzle	Configuration	M_d	D_e - in	NPR_d
smc000	Convergent	1.00	2.0	1.89
smc021*	Convergent	1.00	2.0	1.89
smc014	CD	1.185	2.0	2.37
smc015	CD	1.40	2.0	3.18
smc016	CD	1.50	2.0	3.67
smc018	CD	1.80	2.0	5.74

* convergent nozzle with reduced screech

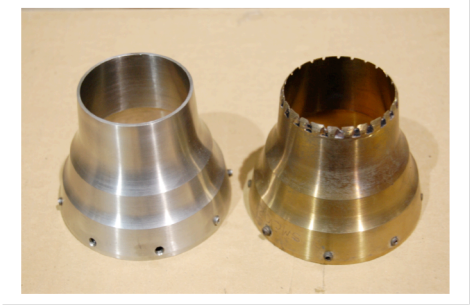

Fig. 1.3 smc000 and smc021 nozzles.

1.3 Mixing Noise and Velocity Power Factors

Power laws for the jet mixing noise are derived from a matrix of test cases that are free of shock-associated noise. A convergent nozzle (i.e. smc000, Table 1.1) operating at a nozzle pressure ratio NPR < 1.89 is considered for this purpose. A set of *N* test cases is tabulated at each temperature (either static or stagnation temperature), where each case corresponds to an exit velocity $U_i, i = 1,2,...,N$. Measurements are reported on a 100-diameter (200-inches) arc, and at 24 equally spaced angles θ (50^o to 165^o relative to the nozzle inlet).

The integrated spectrum (i.e. the overall sound pressure level OASPL) at each jet velocity U_i is

$$\hat{y}_i = OASPL(\theta,T), \quad i = 1,2,...,N \tag{1.1}$$

The integration is carried out in a narrow-band, and within a fixed Strouhal frequency range after removing possible extraneous facility noise at either low- or high-end of the spectrum. Since $\hat{y}_i$ depends on the integration band limits, two independent set of calculation are presented at pre-selected Strouhal ranges of $0.10 \le St \le 5.0$ and $0.02 \le St \le 10.0$. Depending on the frequency range selected, the dB difference between the respective $\hat{y}_i$ values is of the order of 1.50 dB or less.

Using a linear least squares regression method, we define a line-fit

$$y_i = n(\theta,T)\,x_i + B(\theta,T); \quad x_i = 10Log(U_i / c_\infty), \quad i = 1,2,...,N \tag{1.2}$$

n and *B* are referred to as the velocity power factor and the intercept parameter respectively. The intercept parameter *B* is the same as the approximated overall sound pressure level directivity (OASPL) at temperature *T* if the exit acoustic Mach number were 1.0. Subsequently the effect of the arc distance on noise is also included in parameter *B*. As pointed out earlier, all measurement presented in this report are at an arc distance of 100*D* and are corrected for atmospheric attenuation as well.

Let the uncertainty at each data point be σ_i; then the measure of goodness of the fit is defined as

$$\chi(\theta,T) = \frac{1}{N-2}\sum_{i=1}^{N}\frac{(\hat{y}_i - y_i)^2}{\sigma_i}. \tag{1.3}$$

We require *N* to be at least 3.0. Additionally, all experimental data are considered to have equal uncertainty $(\sigma_i = 1)$. Sample examples are given in the following sections that examine the confidence intervals for regression parameters *n* and *B* at several angles of interest.

1.4 Power Law at Constant Static Temperature

Table 1.2 lists a selection of SHJAR readings at constant static temperatures of T_s =1.0, 1.20, 1.43, 1.76, 2.27, 2.70. Set points are listed in the order of increasing Mach number. Special care has been taken to limit all set points to a class of subsonic Mach number in order to exclude the shock-associated noise. Several temperature readings consist of set points at supersonic acoustic Mach number (i.e. M_a > 1.0), highlighted in gray. It will be shown that the velocity power factor *n* is most sensitive to the exclusion of these set points at aft angles.

As a first exercise, the highlighted readings are excluded from the least squares method, and the number of samples is set at *N* = 3,3,5,6,6,4 at the respective temperatures. We also choose to integrate the spectra in the frequency range $0.10 \le St \le 5.0$. The results are shown in Fig. 1.4 as a set of parametric curves for

velocity power factor $n(\theta,T)$ and the intercept parameter $B(\theta,T)$. Figure 1.5 shows that the goodness factor $\chi(\theta,T)$, for the most part, remains relatively close to 0.0 indicating small data scatter at all angles.

Table 1.2 Selected SHJAR readings at constant static temperature T_s

Rdg	T_s	T_t	M_a	M	NPR	$\mathrm{Re}\times 10^{-5}$
1521	1.0	1.04	0.50	0.50	1.18	5.89
1523	1.0	1.10	0.70	0.70	1.38	8.24
1524	1.0	1.16	0.90	0.90	1.69	10.60
1528	1.20	1.25	0.50	0.45	1.153	4.27
1529	1.20	1.30	0.71	0.64	1.318	6.06
1530	1.20	1.36	0.90	0.82	1.563	7.69
5619	1.42	1.45	0.39	0.33	1.078	2.46
5621	1.42	1.49	0.59	0.50	1.184	3.72
5622	1.42	1.52	0.69	0.58	1.257	4.35
5623	1.43	1.55	0.79	0.66	1.339	4.98
5624	1.43	1.59	0.89	0.75	1.451	5.62
5627	1.43	1.71	1.18	0.98	1.857	7.45
5615	1.76	1.79	0.39	0.29	1.06	1.73
5578	1.76	1.81	0.49	0.37	1.099	2.16
5614	1.76	1.83	0.59	0.45	1.146	2.60
5613	1.76	1.86	0.69	0.52	1.20	3.04
5612	1.76	1.88	0.79	0.60	1.274	3.48
5579	1.76	1.92	0.89	0.67	1.35	3.92
5629	1.76	2.04	1.18	0.89	1.667	5.20
5580	1.76	2.11	1.32	1.0	1.890	5.81
5599	2.27	2.30	0.39	0.26	1.04	1.13
5600	2.27	2.31	0.49	0.33	1.076	1.42
5601	2.27	2.33	0.59	0.39	1.11	1.71
5602	2.27	2.36	0.68	0.46	1.15	1.97
5603	2.27	2.39	0.79	0.53	1.20	2.28
5605	2.27	2.42	0.89	0.59	1.264	2.57
5607	2.27	2.52	1.15	0.77	1.472	3.33
5608	2.27	2.61	1.32	0.88	1.648	3.82
5611	2.27	2.69	1.47	0.98	1.844	4.25
5585	2.70	2.73	0.39	0.24	1.04	0.85
5586	2.71	2.77	0.59	0.36	1.09	1.28
5587	2.71	2.80	0.69	0.42	1.12	1.50
5588	2.70	2.81	0.79	0.48	1.17	1.72
5590	2.71	2.97	1.17	0.72	1.40	2.55
5592	2.71	3.03	1.32	0.81	1.52	2.87
5581	2.70	3.09	1.47	0.91	1.69	3.20

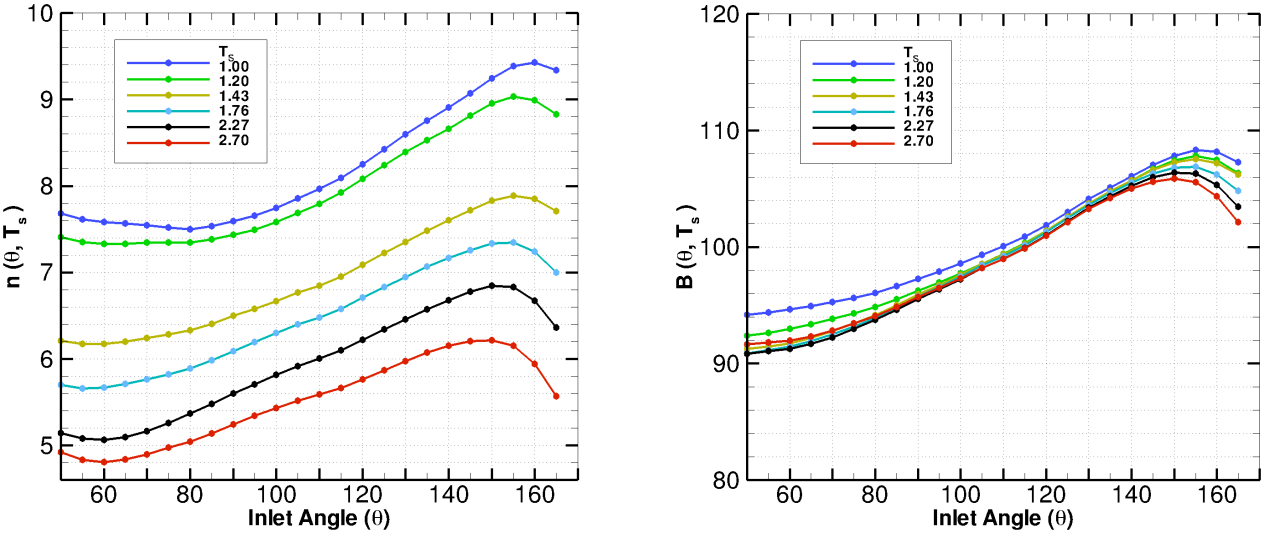

(a) (b)

Fig. 1.4 Velocity power factor (part a) and the intercept parameter (part b) at constant static temperature and with Strouhal limits of 0.10<St<5.0. (Least squares regression at subsonic points of Table 1.2.)

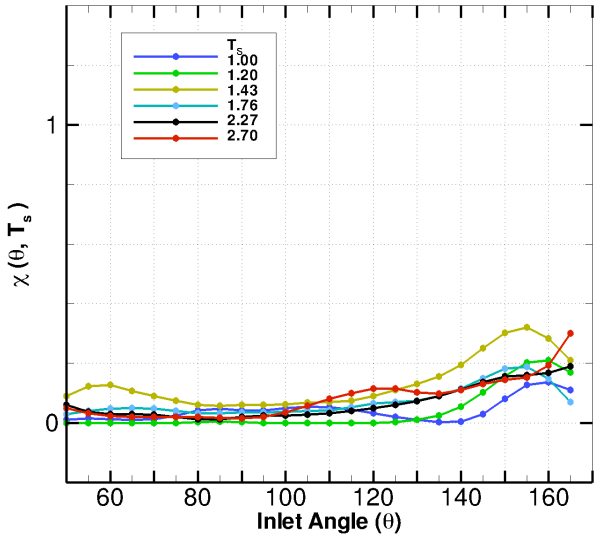

Fig. 1.5 Goodness factor $\chi(\theta,T)$ related to Fig. 1.4

As an example, consider a jet at an acoustic Mach number of $M_a = 0.590$, and static temperature ratio of $T_s = 2.70$. The measured OASPL at, say $\theta = 60^o$, is 80.81 dB. Figures 1.4 shows that at this angle and temperature, the parameters of interest are $n = 4.79, B = 91.72$. Therefore, according to regression formula 1.2 we approximate the area under the spectrum as

$$y = 47.9 Log(0.590) + 91.72 = 80.74\, dB\,,$$

which is only 0.07 dB away from the measurements. The 95% confidence band [Ref. 17] for the regression parameter y_i using the 5% quantile of Fisher's F distribution and a 4-points regression at $T_S = 2.70$ is within the dashed-lines in Fig. 1.6. For this particular point, the band is determined as $80.74 \pm 0.40\,dB$. Note that in the bandwidth is not uniform and it could be as large as 0.90 dB at the two limits of the abscissa shown in Fig. 1.6. A 95% joint confidence region for parameters n and B is an ellipsoid as shown in Fig. 1.7 (part a). The dashed lines show the inference intervals for the two parameters as $B = 91.72 \pm 0.72$ and $n = 4.79 \pm 0.28$. The confidence area shrinks with decreasing the confidence percentage to 90% as seen in part b of Fig. 1.7.

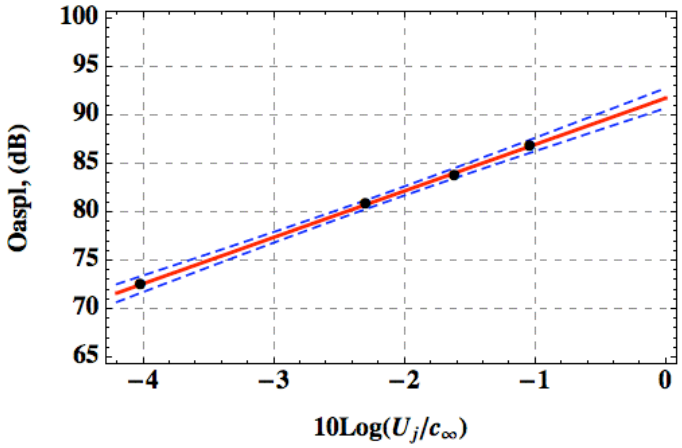

Fig. 1.6 Measurements (symbols); least squares fitted line (red); and the 95% confidence band (dashed lines). $T_s = 2.70, \theta = 60^o$ **and** $0.10 \le St \le 5.0$**.**

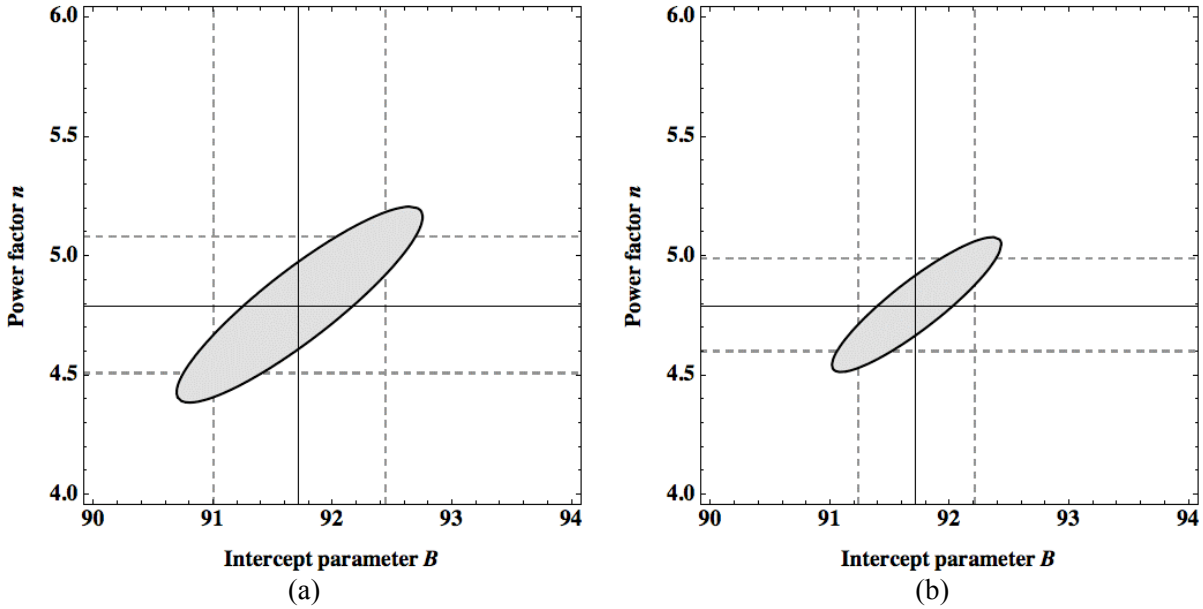

Fig. 1.7 Joint confidence region (ellipsoid) and marginal inference intervals (dashed lines) of parameters *n* and *B* at: (a) 95% confidence ; (b) 90% confidence. (Least squares regression at subsonic points of Table 1.2 at $T_s = 2.70, \theta = 60^o$ **and** $0.10 \le St \le 5.0$**.)**

When the calculations are repeated at $\theta = 160^{O}$, we find an approximated value of $y = 90.91\text{dB}$, vs. the experimental value of 90.66 dB. However, the 95% confidence band around the line fit and the marginal inference intervals for the regression parameters (Fig. 1.8a and b) are noticeably larger compared to those at 60°. The 95% inference intervals are estimates as $B = 104.72 \pm 1.90$ and $n = 6.0 \pm 0.78$.

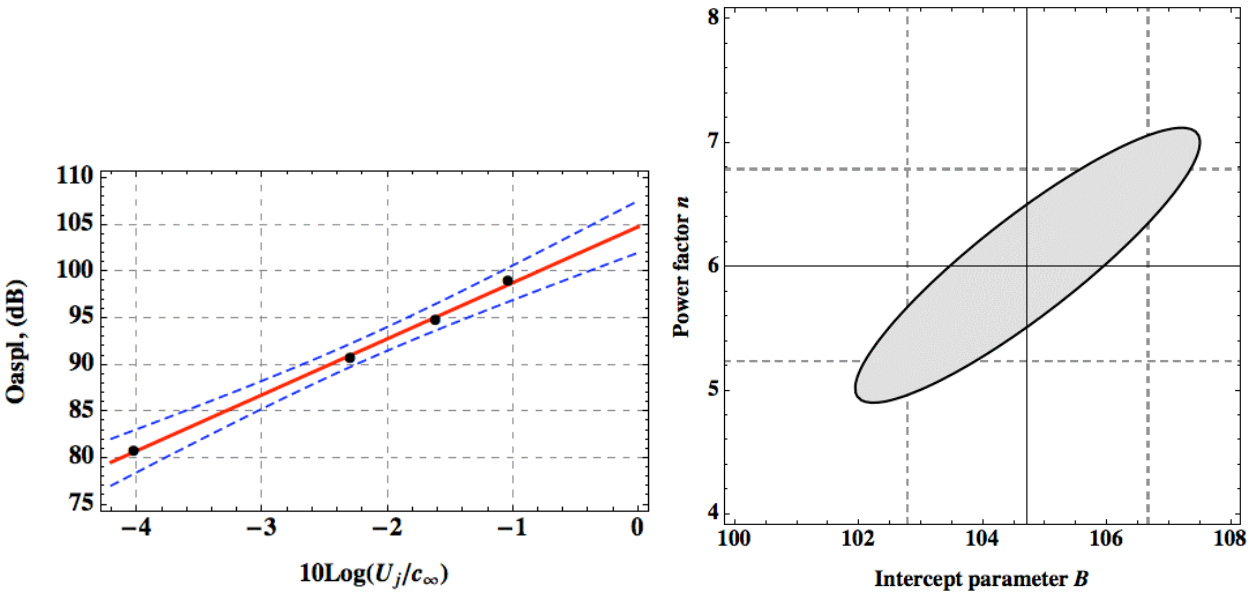

(a) (b)

Fig. 1.8 (a): Measurements (symbols); least squares fitted line (red); and the 95% confidence band (dashed lines); (b): Joint 95% confidence region (ellipsoid) and marginal inference intervals (dashed lines) of parameters *n* and *B*. (Least squares regression at subsonic points of Table 1.2 at $T_s = 2.70, \theta = 160^{o}$ and $0.10 \le St \le 5.0$.)

In order to examine other possible sources of the uncertainty at a range of jet speeds, typical jet noise spectra at two angles of 90° and 150° are illustrated in Fig. 1.9. It is seen that both the peak Strouhal frequency and the relative amplitude decay from the peak (within a selective frequency band) change with angle and speed. Therefore, it would be curious to pose the following questions:

(1) How would the regression results be different if the spectral range were to extend beyond $0.10 \le St \le 5.0$? Would the two parameters be significantly different from that shown in Fig. 1.4?

(2) What if the set points were to extend into supersonic acoustic Mach numbers? Would the goodness factors and the confidence intervals change noticeably that should render the regression scheme as doubtful or perhaps useless at some angles?

The first question is answered when we chose an extended frequency range $0.02 \le St \le 10.0$ to integrate the spectrum. Figures 1.10 and 1.11 show the respective parameters *n* and *B* and the goodness factor χ. Compared to the earlier estimates shown in Fig. 1.4, the velocity power factors are slightly different (of the order of 0.30 or less), but changes are not uniform and depend on both angle and temperature.

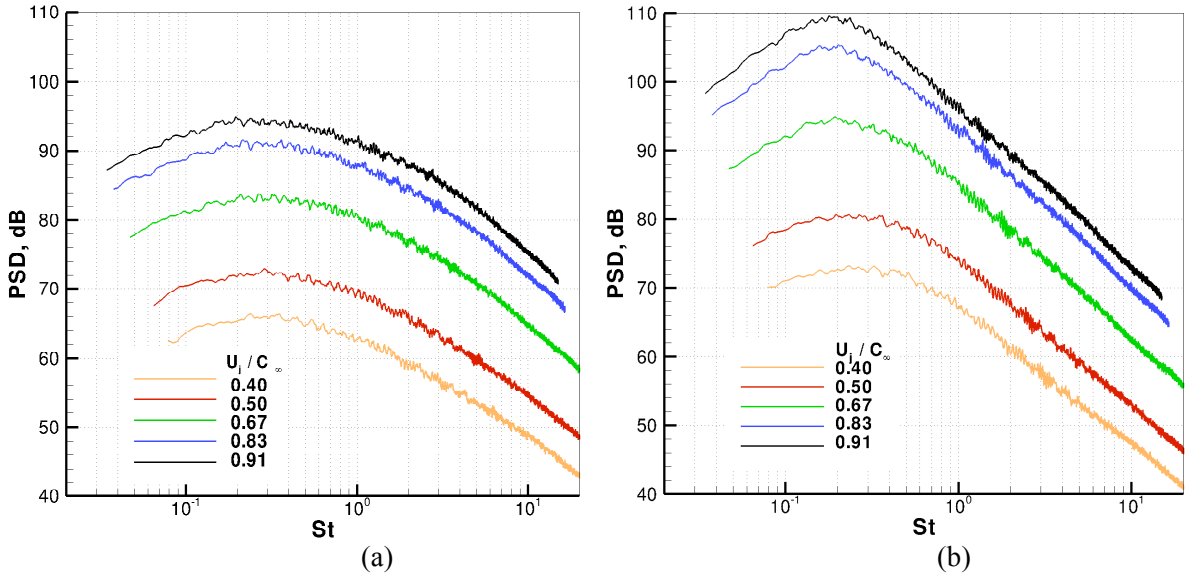

Fig. 1.9 Power spectral density at 90° (part a), and 150° (part b), at indicated acoustic Mach numbers in the smc000 nozzle at T_t = 1.0.

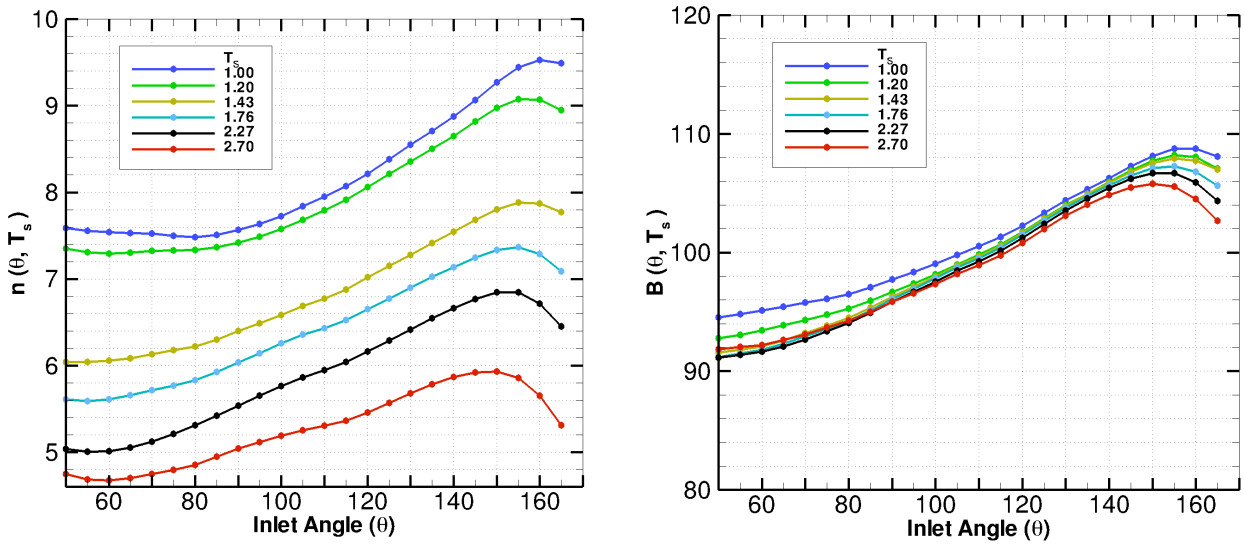

Fig. 1.10 Velocity power factor *n* (part a) and the intercept parameter *B* (part b) at constant static temperature and with Strouhal limits of 0.02<St<10.0. (Least squares regression at subsonic points of Table 1.2.)

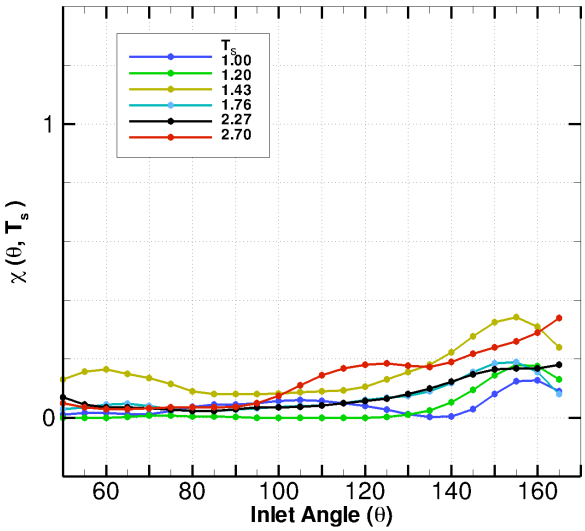

Fig. 1.11 Goodness factor $\chi(\theta,T)$ related to Fig. 1.10

The intercept parameter (Fig. 1.10 part b) is expected to be somewhat larger due to the additional area under the spectrum (i.e. 0.20 to 1.50 dB), subsequently *n*-factors change accordingly. It is readily shown that parameters *n* and *B* as selected from Fig 1.10 predict the OASPL at the four regression points to within 0.40 dB at all angles and temperatures. Although the goodness factor remains small as before (Fig. 1.11), the 95% confidence region at 160^{o} deteriorates slightly as the marginal inference intervals expand to within $B = 104.84 \pm 2.60$ and $n = 5.71 \pm 1.02$ (see Fig. 1.12). A reduction of 0.29 in the central value of *n* is also noticeable compared to the earlier estimates with a more restrictive Strouhal frequency. In general, an extended frequency range better represents the OASPL, and should be considered as a preferred selection provided that the data quality is not compromised at the two frequency limits.

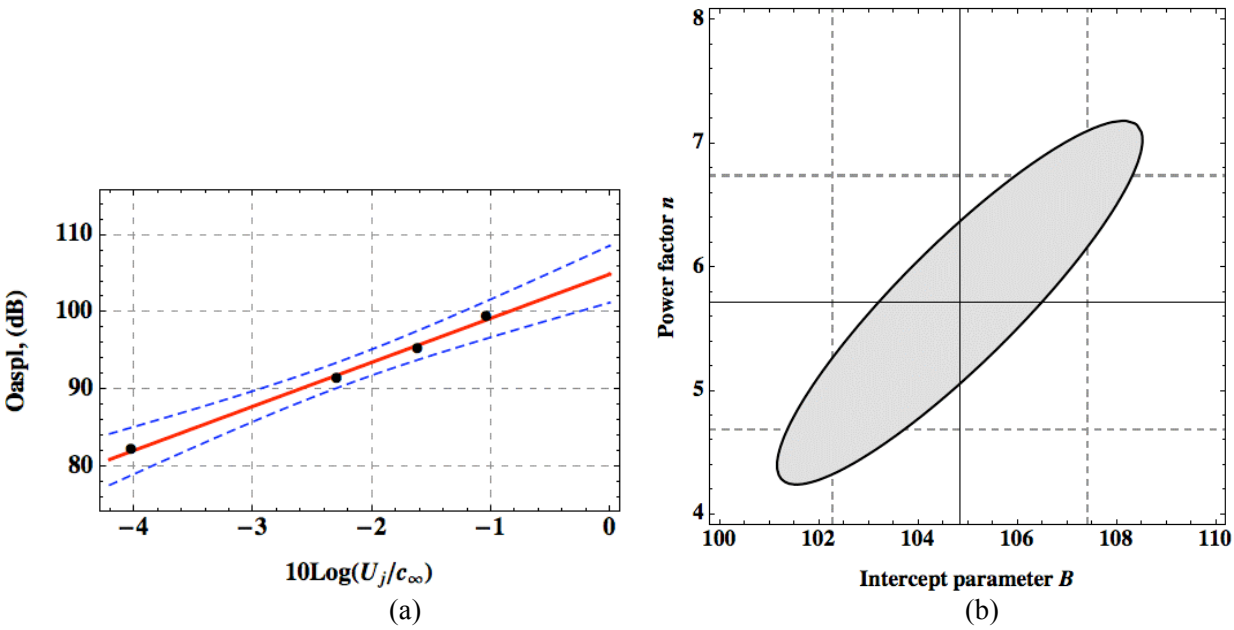

Fig. 1.12 **(a): Measurements (symbols); least squares fitted line (red); and the 95% confidence band (dashed lines); (b): Joint 95% confidence region (ellipsoid) and marginal inference intervals (dashed lines) of parameters *n* and *B*. (Least squares regression at subsonic points of Table 1.2 at $T_s = 2.70, \theta = 160^o$ and extended frequency range of $0.02 \le St \le 10.0$.)**

To answer the second question, we add set points highlighted in gray to the matrix of the interpolation points. Note that the aerodynamic Mach number is still subsonic at all conditions. The calculations are repeated within a Strouhal frequency range of $0.02 \le St \le 10.0$ as shown in Figs 1.13 and 1.14.

The power factors in Fig. 1.13 are now compared with the earlier calculations in Fig. 1.10. Parametric curves at $T_s = 1.0$ and 1.2 are unaffected since they use the same regression points as before. However, there seems to be a dramatic change in the spatial distribution of *n*-factors at aft angles. Parametric curves appear to converge in the vicinity of 150^o, and depart drastically from earlier estimates of Fig. 1.10 that projected a rather parallel distribution throughout the angle range. If higher speed jets with supersonic aerodynamic Mach number were also included in the regression, the convergence of the parametric curves would become stronger (see Fig. 16, [Ref. 3]). Along the sideline and inlet angles, however, the earlier distribution is more or less maintained, with the exception of a slight vertical shift of 0.10 to 0.20 in lieu of the new intercept parameter.

As expected, addition of the new test points to a regression scheme should narrow down the confidence band surrounding the least squares line fit as long as that the data scatter remains small. When the variance is large, (as seen in Fig. 1.14, at $\theta \ge 120^o$), the changes in the confidence region are either marginal or are for the worse. To demonstrate this, the 95% confidence band, and the joint confidence region related to parameters *n* and *B* are evaluated at two angles of 60^o and 160^o using a 7-points regression at T_s =2.70. The 60^o results (see Fig. 1.15) improve relative to the earlier estimates with 4 points and the marginal inference intervals for *n* and *B* reduce to ±0.16 and ±0.32 respectively. Similar error band analysis at 160^o (Fig. 1.16) shows that, even in the light of a slight reduction in the confidence region relative to the 4-point regression results, the inference intervals still remain quite high owing to the increased data scatter at this angle (±0.70 and ±1.46 for *n* and *B* respectively).
The above error estimates point to the deteriorating quality of the regression process at aft angles as a result of increased data scatter at supersonic speeds.

It will be shown later on that changes in the spectral shape with jet speed at aft angles make it increasingly difficult to obtain a satisfactory spectral collapse throughout the frequency range at all speeds. However, the regression parameters *n* and *B*, as shown in Fig. 1.13, could still be employed to collapse, at least, a major segment of the subsonic data at aft angles. The collapsed segments correspond to the high frequency roll-off of the pressure amplitude. If this spectral element is attributed to a particular source component, then it could also be scaled up to the velocity of a supersonic jet and be viewed as one component of noise at such speeds. The supersonic jet noise spectra at aft angles may subsequently be considered as superposition of two incoherent components.

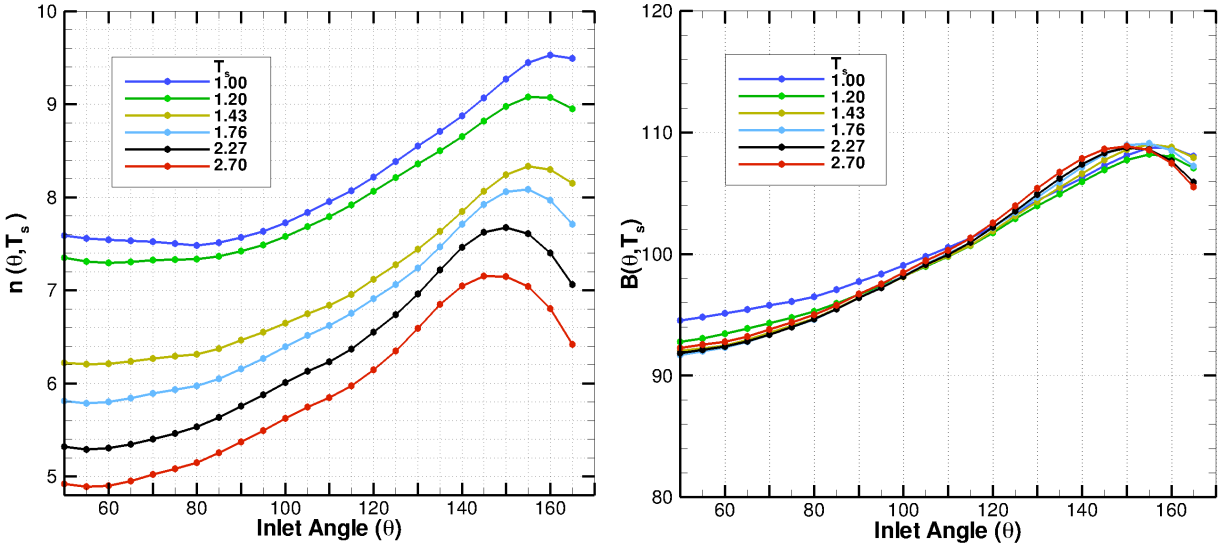

(a) (b)

Fig. 1.13 Velocity power factor *n* (part a) and the intercept parameter *B* (part b) at constant static temperature and with Strouhal limits of 0.02<St<10.0. (Least squares regression – including supersonic points of Table 1.2)

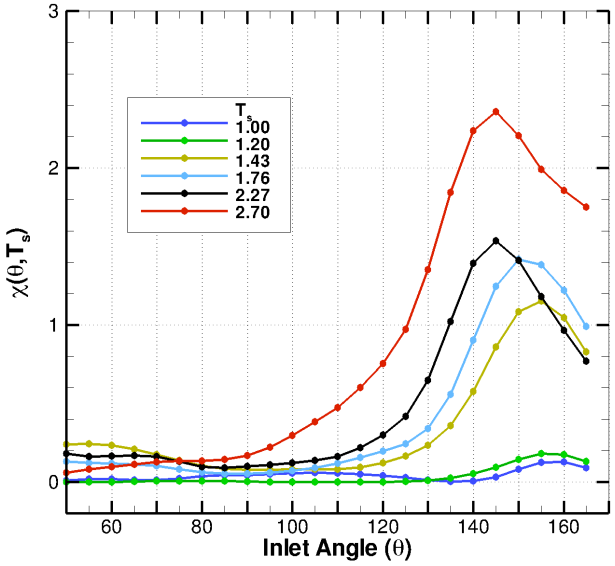

Fig. 1.14 Goodness factor as related to figure 1.13

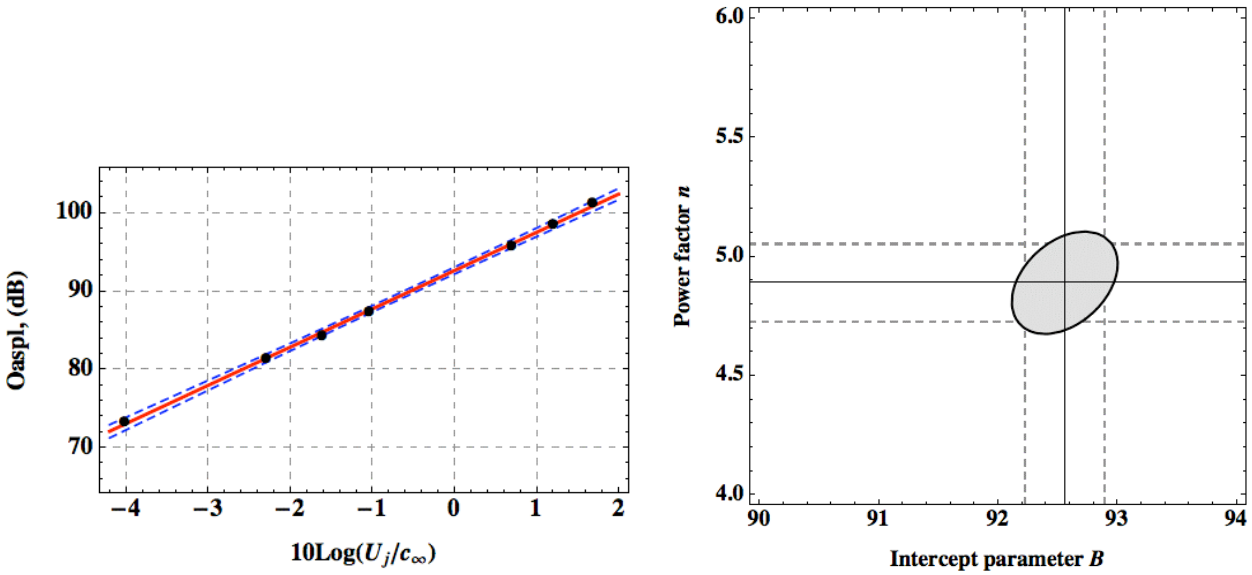

(a) (b)

Fig. 1.15 **(a): Measurements (symbols); least squares fitted line (red); and the 95% confidence band (dashed lines); (b): Joint 95% confidence region (ellipsoid) and marginal inference intervals (dashed lines) of parameters *n* and *B*. (Least squares regression at $T_s = 2.70, \theta = 60^o$ using extended frequency range of $0.02 \le St \le 10.0$ – and including supersonic points of Table 1.2)**

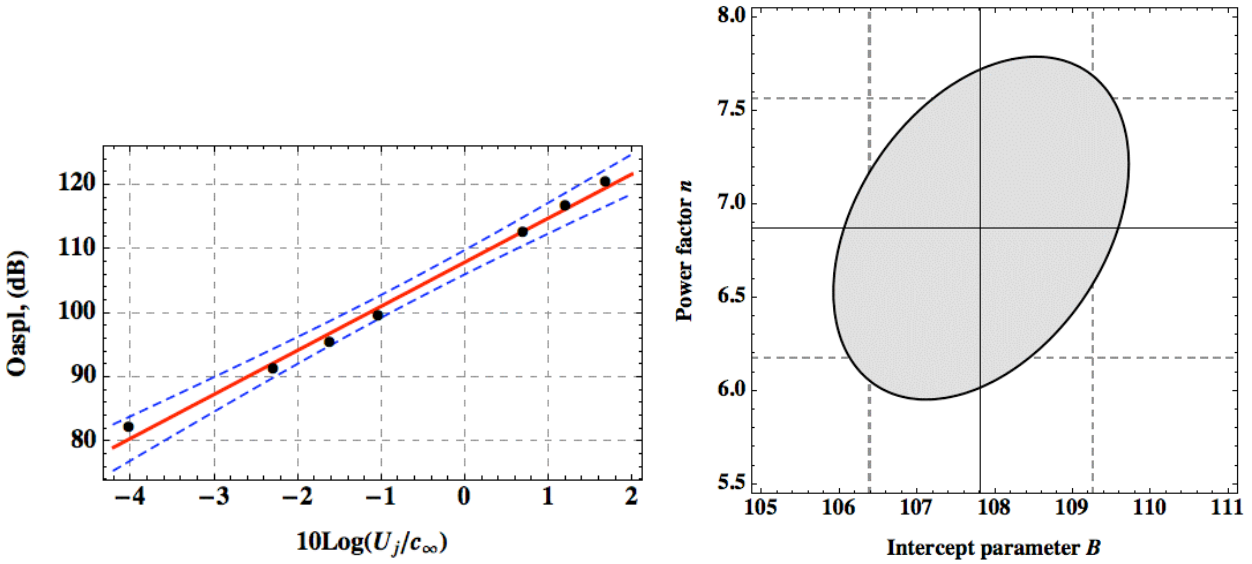

(a) (b)

Fig. 1.16 **(a): Measurements (symbols); least squares fitted line (red); and the 95% confidence band (dashed lines); (b): Joint 95% confidence region (ellipsoid) and marginal inference intervals (dashed lines) of parameters *n* and *B*. (Least squares regression at $T_s = 2.70, \theta = 160^o$ using extended frequency range of $0.02 \le St \le 10.0$ – and including supersonic points of Table 1.2)**

1.5 Power Law at Constant Stagnation Temperature

The linear regression discussed in the previous section is now implemented at a constant stagnation temperature. The set of conditions selected for this exercise is shown in Table 1.3. Some set points consist of a supersonic acoustic Mach number (highlighted in gray shade). We follow a similar approach as before and develop a template free of the supersonic conditions initially, with readings N = 5,3,3,3 at temperatures T_t = 1.0,1.8,2.2,2.7 respectively. For this exercise, the power spectral density is integrated within the extended frequency range $0.02 \le St \le 10.0$. Earlier, it was shown that the confidence band and marginal inference intervals for parameters n and B vs. static temperature and angle deteriorated at aft angles as higher speed test points were added to the set of regression points. We skip the error estimates here and assume that similar conclusions hold as before, and simply present the regression parameters with and without the supersonic points.

Table 1.3 Selected readings at constant stagnation temperature T_t

Rdg	T_s	T_t	M_a	M	NPR	$\mathrm{Re}\times 10^{-5}$
1610	0.97	1.0	0.40	0.40	1.117	4.98
1611	0.96	1.0	0.49	0.50	1.186	6.22
1612	0.91	1.0	0.67	0.70	1.387	9.36
1613	0.86	1.0	0.83	0.90	1.692	12.80
1614	0.83	1.0	0.91	1.00	1.893	15.11
1579	1.74	1.8	0.52	0.40	1.117	2.35
1581	1.70	1.8	0.65	0.50	1.186	3.06
1582	1.65	1.8	0.89	0.70	1.387	3.58
1583	1.56	1.8	1.12	0.90	1.69	6.11
1584	1.50	1.8	1.22	1.0	1.89	7.12
1568	2.13	2.2	0.58	0.40	1.117	1.88
1569	2.10	2.2	0.72	0.50	1.186	2.39
1570	2.00	2.2	0.99	0.70	1.387	3.56
1571	1.91	2.2	1.24	0.90	1.69	4.81
1572	1.83	2.2	1.36	1.0	1.89	5.66
1561	2.62	2.7	0.64	0.40	1.117	1.47
1562	2.58	2.7	0.80	0.50	1.186	1.89
1563	2.47	2.7	1.09	0.70	1.387	2.77
1564	2.35	2.7	1.37	0.90	1.69	3.77
1565	2.26	2.7	1.50	1.0	1.89	4.41

The scaling law parameters n and B are shown in Fig. 1.17 (a and b). Although data scatter in Fig. 1.18 remains small, the 95% confidence region could be improved only when more points are added. Additional readings at supersonic conditions (i.e. shaded points in Table 1.3) are now added to the least squares regression fit. The results are shown in Figs. 1.19 to 1.20. As before, along the sideline angles the 95% confidence band surrounding the line fit is expected to improve (i.e. band interval would decrease). A rise in data scatter at aft angles, however, leads to a noticeable increase in the goodness factor (Fig. 1.20), and adversely affects the quality of the linear regression near the downstream jet axis.

An interesting observation that separates the unheated and heated jets is a near collapse of the intercept parameter B for all heated jets illustrated in Fig. 1.19b. The intercept parameter B is seen distinctly discrete for the unheated jet. When plotted as a function of static temperature (see Fig. 1.13b), even at the smallest static temperature ratio of T_s=1.0 the jet is slightly heated according to $T_t = T_s + (\gamma - 1)M_a^2/2$. It was pointed out earlier that the intercept parameter B represents the OASPL directivity at a given temperature when $M_a = 1.0$. At an acoustic Mach number of 1.0, the two temperatures relate per one-

dimensional flow relation $T_t = T_s + 0.20$, therefore there is a correspondence between parametric curves in Figs. 1.13b and 1.19b at similar temperatures. For example, $B(\theta, T_t = 1.20)$ (not shown in Fig. 1.19b) should look like $B(\theta, T_s = 1.0)$ in Fig. 1.13b because both curves represent the OASPL at identical flow conditions. A similar correspondence between the *n*-factors at the two temperatures is not possible simply because we cannot fix the acoustic Mach number to convert temperatures.

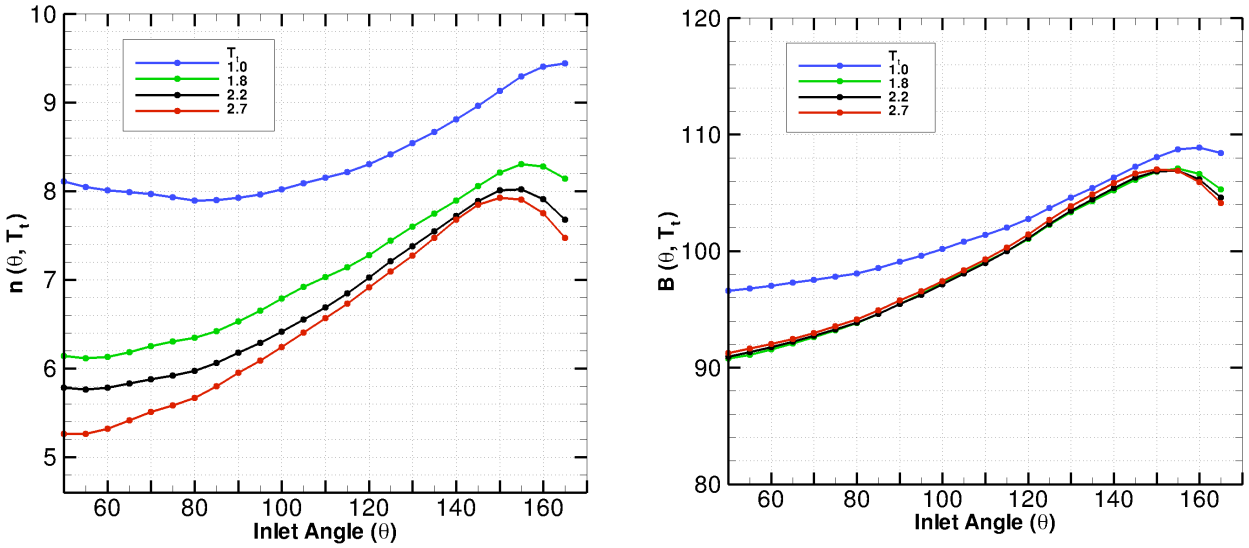

Fig. 1.17 Velocity power factor *n* (part a) and the intercept parameter *B* (part b) at constant stagnation temperature. (Least squares regression at subsonic points of Table 1.3.)

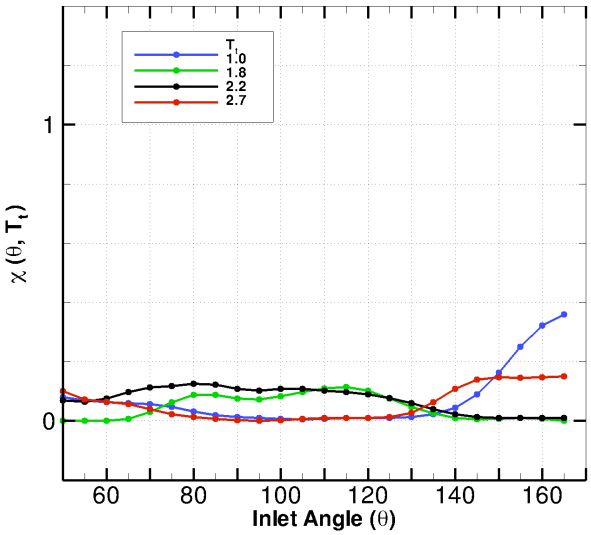

Fig. 1.18 Goodness factor related to Fig. 1.17

In section 2, we will examine the spectral collapse of the jet noise data using the scaling parameters n and B. It will be shown that only one parameter, i.e. velocity power factors n, will suffice when spectral data is scaled across jets of equal temperature (either static or stagnation). Jets with different temperatures require both parameters n and B, as delta-dB in the B values at the two temperatures also enters the scaling relation. But Fig 1.19b shows that at three temperatures of T_t =1.8, 2.2 and 2.7, delta-dB in parameter B is quite small as long as $\theta \le 140^o$. Subsequently only parameter n would suffice to achieve a successful scaling across these temperatures. Addition of extra heat will not change the OASPL at such angles when the acoustic Mach number is held fixed at 1.0. A similar statement does not hold true across lower heated jets (see Fig. 1.13b for parameter B vs. static temperature). Application of the scaling laws across heated and unheated jets requires both parameters n and B as seen in Figs. 1.13b and 1.19b.

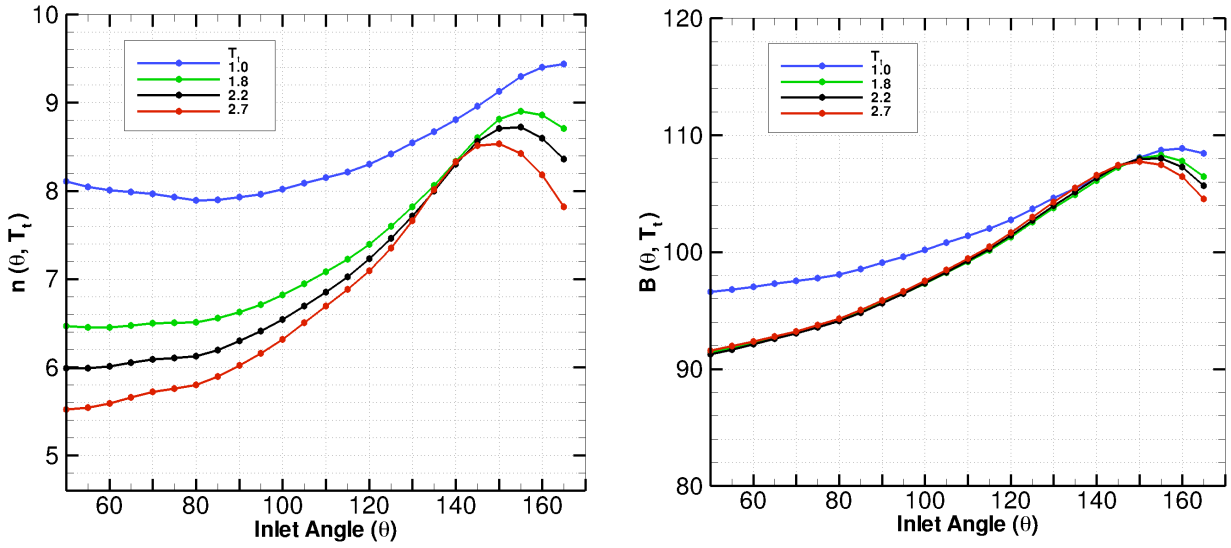

(a) (b)

Fig. 1.19 Velocity power factor n (part a) and the intercept parameter B (part b) at constant stagnation temperature. (Least squares regression includes supersonic points of Table 1.3)

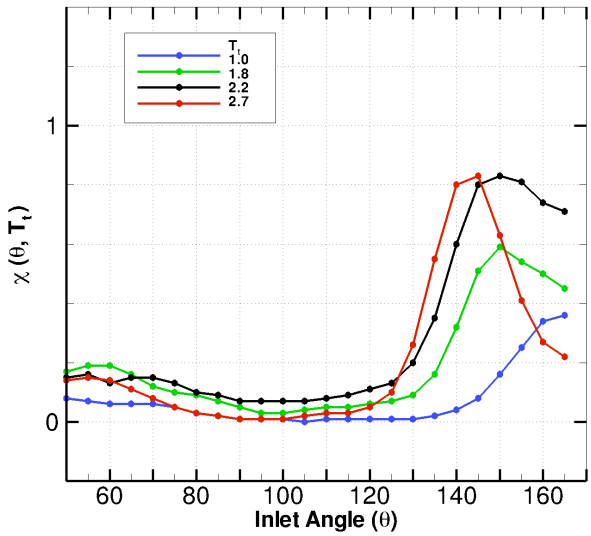

Fig. 1.20 Goodness factor related to Fig. 1.19

The preceding discussions point to the following:

(1) Velocity power factor templates (such as Fig. 1.19) deteriorate at aft angles due to changes in the general shape of the spectrum with jet velocity (see the 150° jet noise spectra in Fig. 1.9b). This will be illustrated further when we examine the jet noise spectra in detail later on. A velocity power factor as calculated from the area under the spectrum should not be expected to collapse the spectral data across a range of Mach numbers at aft angles. With the selection of an appropriate frequency parameter (and subsequent adjustment in parameter *n*, as will be discussed shortly) we may, at best, collapse a segment of the spectra.

(2) Velocity power factors developed around constant static or stagnation temperatures are equally useful when applying the scaling laws. The argument could be put on firm grounds only if the regression confidence margins at a constant stagnation temperature were comparable to those at a constant static temperature. Sample calculations at T_t=2.20, as seen in Figure 1.21, show that even with a 5-points regression (relative to a 7-points regression shown in Fig. 1.15), the two confidence regions at a typical angle of 60° are quite comparable. Since *B* represents the OASPL directivity at M_a=1.0 where the two temperatures convert as $T_t = T_s + 0.20$, then a one-to-one relationship exits between $B(\theta, T_t)$ and $B(\theta, T_s)$ at similar temperatures. A parallel correspondence is not possible between the two *n* factors because velocity cannot be held constant in order to convert temperatures. As seen in Fig. 1.19b, parameter *B* appears to collapse at high temperatures, allowing for the scaling laws to be implemented across such temperatures with a single parameter *n* only. Lower temperature jets, on the other hand, require both parameters *n* and *B* for a successful scaling regardless of which temperature is used.

The major difference between the two temperatures relates to approximations made is defining a single static temperature in a jet when in reality it is affected by changes in the velocity profile. Experimentally, the plenum total temperature is a control parameter, while the static temperature at the jet exit is calculated using one-dimensional Bernoulli's equation for a compressible flow.

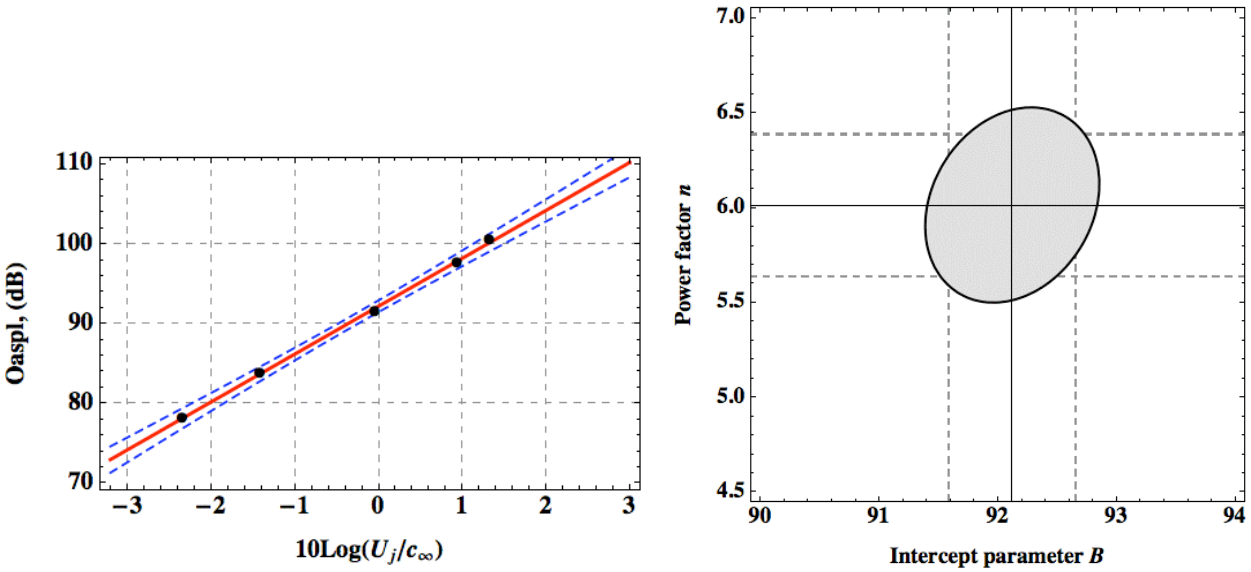

Fig. 1.21 **(a): Measurements (symbols); least squares fitted line (red); and the 95% confidence band (dashed lines); (b): Joint 95% confidence region (ellipsoid) and marginal inference intervals (dashed lines) of parameters *n* and *B*. (Least squares regression at $T_t = 2.20, \theta = 60^o$ using extended frequency range of $0.02 \le St \le 10.0$ – and including supersonic points of Table 1.3)**

2.1 Examination of SHJAR Spectral Data

In the previous section, parametric curves were developed that describe the velocity power factor $n(\theta,T)$, and the intercept parameter $B(\theta,T)$ in a least squares regression. The regression used the OASPL as the dependent variable, and $10Log(U_j/c_\infty)$ as its independent variable. Here we study the spectral collapse at various angles, temperatures, and Mach numbers using a selection of different nozzle geometries. Flow conditions include both subsonic and supersonic jets. The supersonic conditions are divided into two classes of nozzles:

1) A convergent nozzle (such as smc000) is said to be under-expanded when it is operated at a nozzle pressure ratio $NPR = p_t / p_\infty$ that is larger than its design value of $NPR_d = \left((\gamma+1)/2\right)^{\gamma/(\gamma-1)} \cong 1.89$, assuming an ideal gas and $\gamma \simeq 1.40$. Under such conditions, the exit Mach number remains as 1.0, but the jet will expand further outside of the exhaust plane to a supersonic Mach number, referred to as the fully expanded or ideally expanded Mach number M_j

$$NPR = (1+\frac{\gamma-1}{2}M_j^2)^{\frac{\gamma}{\gamma-1}}. \tag{2.1}$$

The corresponding fully expanded static temperature ratio T_s is related to the stagnation temperature ratio T_t

$$T_t / T_s = NPR^{\frac{\gamma-1}{\gamma}}. \tag{2.2}$$

The mismatch between the exit pressure and the ambient static pressure results in shock-cell formation. In practice, we may consider the associated entropy change small enough to allow an estimate of the fully expanded jet area under the isentropic conditions

$$\frac{p}{\rho^\gamma} = const, \quad \text{(isentropic)} \tag{2.3}$$

$$p = \rho RT. \quad \text{(ideal gas)} \tag{2.4}$$

The above equations plus the conservation of mass lead to the following approximate relations between the exit static pressure p_e, the ambient pressure p_∞, the fully expanded jet area A_j, and exit area A_e.

$$\frac{p_e}{p_\infty} = \left(\frac{1+M_j^2(\gamma-1)/2}{1+M_d^2(\gamma-1)/2}\right)^{\frac{\gamma}{\gamma-1}}, \qquad \frac{A_j}{A_e} = \frac{M_d}{M_j}\left(\frac{p_e}{p_\infty}\right)^{\frac{\gamma+1}{2\gamma}}. \tag{2.5}$$

In an under-expanded convergent nozzle the design Mach number is $M_d = 1.0$.

2) A convergent-divergent nozzle (such as smc016, Table 1.1) will reach Mach 1.0 at the throat, and will further expand to a design Mach number M_d at the nozzle exit. The required nozzle pressure ratio is calculated from (2.1) when M_d is substituted for M_j. Similar to the convergent nozzles, when the input

pressure ratio is larger than the design value, a nozzle is called under-expanded. Additional expansion to a new Mach number M_j occurs outside the nozzle. This is usually accompanied with the formation of shock-cell diamonds. Equations 2.1 through 2.5 are applicable as before.

When a CD nozzle operates at a pressure ratio that is less than the design value, shocks are formed inside or outside the nozzle. The nozzle is said to be in an over-expanded mode.

Equation (1.2) may be used to evaluate delta-dB in the OASPL at any angle θ across two different jets. When jets are of equal temperature (static or stagnation), parameter *B* stays the same and scaling from one jet velocity to another depends on parameter *n* and the ratio of the two velocities. If the vertical shift from one power spectral curve to the next equal delta-dB in the respective OASPL, then according to Eq. 1.2 the extra dB associated with U_j^n could be removed from each jet once we define a *scaled PSD*

$$scaled\,PSD \equiv PSD - 10n(\theta,T)Log(U_j / c_\infty) - 10Log(A_j / A_e)\,. \tag{2.6}$$

The scaled spectra are now expected to collapse in amplitude across different jets. The last term in (2.6) signifies that imperfectly expanded supersonic jets reach a fully expanded velocity U_j at jet area A_j as estimated from Eq. (2.5). Power spectral density can also be evaluated as per Helmholtz number $f\,D/\,c_\infty$. Since power spectral density per Helmholtz number converts to that per Strouhal frequency (*PSD*)

$$10Log(\overline{p^2}c_\infty / p_{ref}^2 D) = 10Log(\overline{p^2}U_j / p_{ref}^2 D) - 10Log(U_j / c_\infty)\,, \tag{2.7}$$

then the left hand side of equation (2.6) may also be interpreted as a scaled power spectral density per Helmholtz number provided that *n* is replaced with (*n*+1) on the right hand-side. For brevity, throughout this report, "scaled *PSD*" stands to represent either of the two meanings depending on the selection of the frequency parameter.

2.2 Examination of Data at Constant Stagnation Temperature

Spectral data collapse at four temperature setting of T_t = 1.0, 1.8, 2.2 and 2.7 are illustrated using the velocity power factors of Fig. 1.19. The operation conditions for 9 jets at a constant stagnation temperature ratio of 1.0 are shown in Table 2.1. The first seven readings are due to a convergent nozzle (smc000), with two readings 1616 and 1618 at under-expanded conditions. Reading (1636) is due to a CD nozzle operating at its design condition, i.e. $M_d = 1.50, NPR_d = 3.671$. The last reading (1605) is a convergent nozzle as well (i.e. smc021, Table 1.1), however the nozzle lip is modified with fine notches in order to minimize the screech-related noise at under-expanded conditions.

Table 2.1 SHJAR readings at stagnation temperature ratio 1.0

Rdg	Nozzle	T_s	T_t	U_j / c_∞	M	NPR	M_j	A_j / A_e
1610	smc000	0.97	1.0	0.40	0.40	1.117	0.40	1.0
1611		0.96	1.0	0.49	0.50	1.186	0.50	1.0
1612		0.91	1.0	0.67	0.70	1.387	0.70	1.0
1613		0.86	1.0	0.83	0.90	1.692	0.90	1.0
1614		0.83	1.0	0.91	1.00	1.893	1.00	1.0
1616		0.76	1.0	1.08	1.00	2.556	1.24	1.043
1618		0.70	1.0	1.23	1.00	3.514	1.47	1.156
1636	smc016	0.69	1.0	1.24	1.50	3.671	1.50	1.0
1605	smc021	0.80	1.02	1.04	1.00	2.328	1.17	1.02

Fig 2.1a shows the 90° spectral density for all seven convergent nozzles following scaling law 2.6. With the exception of the under-expanded cases, all spectra collapse at n=7.93 and within the uncertainty of the velocity power factor (see Fig. 1.19 as well as Tables 2.2 and 2.3 for the regression parameters at a constant stagnation temperature).

Table 2.2 Velocity power factor *n* at constant stagnation temperature

θ^o	T_t=1	1.8	2.2	2.7
50	8.11	6.47	5.99	5.52
55	8.03	6.44	5.98	5.53
60	8.01	6.45	6.01	5.59
65	7.99	6.47	6.05	5.66
70	7.97	6.51	6.10	5.73
75	7.94	6.51	6.11	5.76
80	7.87	6.49	6.10	5.78
85	7.90	6.55	6.19	5.89
90	7.93	6.63	6.30	6.02
95	7.95	6.70	6.40	6.15
100	8.02	6.82	6.54	6.31
105	8.09	6.94	6.69	6.50
110	8.16	7.09	6.85	6.70
115	8.20	7.21	7.01	6.87
120	8.30	7.39	7.23	7.09
125	8.41	7.59	7.46	7.33
130	8.55	7.82	7.70	7.65
135	8.66	8.05	7.99	8.02
140	8.81	8.33	8.32	8.37
145	8.95	8.62	8.59	8.56
150	9.13	8.85	8.75	8.56
155	9.31	8.93	8.75	8.45
160	9.43	8.90	8.64	8.23
165	9.44	8.71	8.36	7.82

Table 2.3 Intercept parameter *B* at constant stagnation temperature

θ^o	T_t=1	1.8	2.2	2.7
50	96.59	91.45	91.28	91.58
55	96.73	91.76	91.65	91.95
60	97.07	92.21	92.12	92.36
65	97.28	92.63	92.56	92.75
70	97.51	93.10	93.05	93.21
75	97.84	93.63	93.59	93.76
80	97.97	94.06	94.03	94.25
85	98.53	94.85	94.80	95.02
90	99.14	95.70	95.68	95.88
95	99.55	96.39	96.40	96.60
100	100.17	97.28	97.31	97.50
105	100.83	98.24	98.30	98.48
110	101.38	99.15	99.24	99.44
115	101.95	100.10	100.22	100.43
120	102.72	101.24	101.38	101.59
125	103.70	102.58	102.74	102.98
130	104.68	103.84	104.03	104.34
135	105.37	104.84	105.10	105.47
140	106.30	106.10	106.36	106.66
145	107.25	107.32	107.50	107.56
150	108.13	108.16	108.13	107.87
155	108.81	108.44	108.19	107.64
160	109.16	108.13	107.61	106.80
165	108.43	106.47	105.67	104.54

The two under-expanded jets at readings 1616 and 1618 are both accompanied with shock-associated noise as well as screech. Shock noise is generated due to the interaction of turbulence with the shock cell structures under imperfectly expanded conditions. It is broadband and dominates the spectra at mid- to high frequency, mostly at forward and sideline angles. The screech tones appear as spikes in the spectra. When screech in minimal, the jet mixing noise dominates the spectra at low frequency even in the presence of shock-associated noise. The lack of collapse of under-expanded spectral data to the level of a fully expanded jet at low frequency, as seen in Fig 2.1a, is attributed to the amplification of the jet mixing noise due to screech. An amplification of ~ 4.0 dB is noted in this case. The amplification is present throughout the spectrum. As pointed out in the introduction, we consider the screech-related amplification of the mixing noise as an element of the broadband shock noise.

In the absence of screech, the 90^o spectra are expected to collapse at low frequency. To demonstrate this, consider Fig 2.1b that shows a CD nozzle as well as the reduced-screech convergent nozzle smc021 in addition to the baseline convergent nozzle. Although the CD nozzle is operating at its design condition (i.e. reading 1636 Table 2.1), in practice it is difficult to control the nozzle conditions for a perfectly expanded jet. Small deviations from the design pressure ratio are not uncommon even under carefully monitored conditions – resulting is several decibels of shock-related noise. The collapse of data at low frequency for all three aforementioned nozzles, as seen in Fig 2.1b, confirms the earlier assertion related to the role of screech in amplifying the jet mixing noise.

It is noted that such amplifications need to be removed from data prior to validation or calibration of jet mixing noise prediction methods.

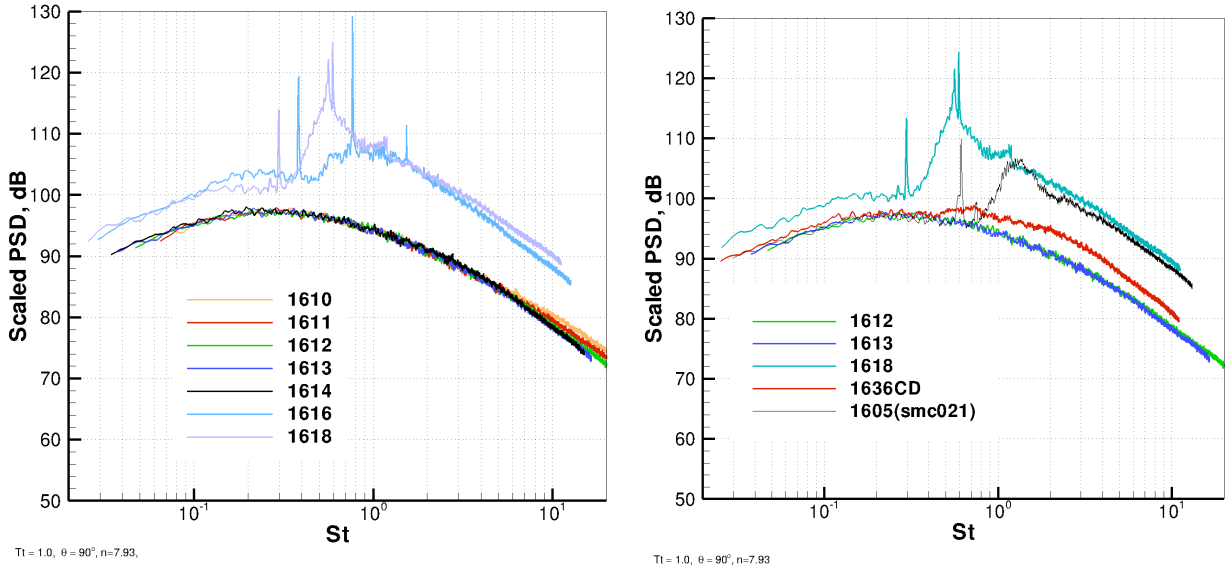

(a) (b)

Fig. 2.1 Application of power law at jet conditions of Table 2.1 ($T_t = 1.0, \theta = 90^o$, n= 7.93.) **(a) smc000 nozzle; (b) a selection of different nozzles.**

Using the power factor $n(\theta,T)$, the scaled spectral data are also displayed at several other angles of common interest. Figure 2.2 demonstrates that shock-associated noise weakens as observer is moved progressively towards aft angles. Screech tones, on the other hand, appear to equally amplify the jet mixing noise at all angles.

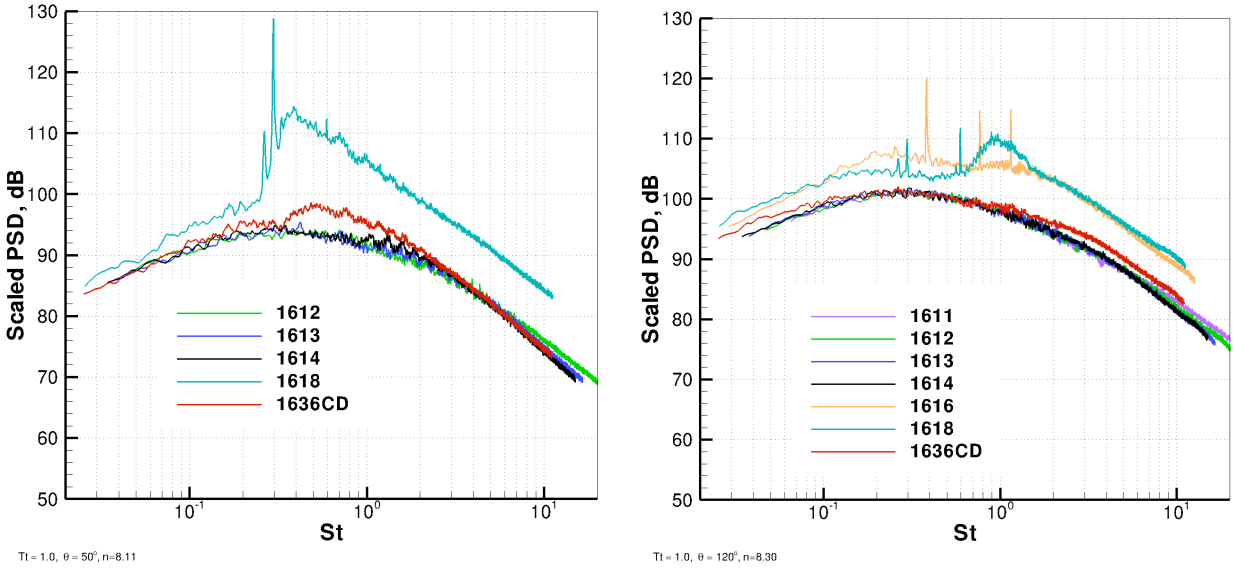

(a) (b)

Fig. 2.2 Application of power law at T_t=1 and jet conditions of Table 2.1
(a) $\theta = 50^o$, n= 8.11; (b) $\theta = 120^o$, n=8.30.

2.3 Collapse of Spectral Data at Aft Angles

Two fundamental assumptions are buried in the spectral power law described in Eq. 2.6. In the first place, it is implied that the basic shape of the spectrum at any angle θ, described by the first term on the right, is invariant with respect to jet velocity and temperature. Second, since the spectral density is expressed as a function of the jet Strouhal frequency, spectra are assumed to peak at the same Strouhal number. When any of these assumptions are violated, data will collapse poorly, and other measures are necessary to fix that.

Figure 2.3a illustrates an attempt to collapse the subsonic noise data at 150°. An inspection of the jet noise data confirms that neither of the rules cited above hold at this angle. The spectra appear relatively wider at lower jet speeds, and display a broader peak. Higher speed jets, on the other hand, exhibit a well-defined peak. It is readily demonstrated that removing the lowest speed jet from the group would increase the value of the power factor n from 9.13 to 9.32. Removing the second lowest speed jet will still increase n to 9.72. This is expected, as the area under the spectrum (on a Log basis) is highly dominated by the peak. When the peak covers a wider span, that particular jet would have an exaggerated effect on the power factor. The goodness factor described in the previous section remains small only when the general shape of the spectrum is preserved. Second, the peak Strouhal frequency is seen to vary between 0.18 and 0.35.

Both problems are fixed once we select the Helmholtz number as the normalized frequency parameter and increment the velocity power factor from 9.13 to 10.13 (as explained in Eq. 2.7). The ordinate in Fig 2.3b represents the spectral density per Helmholtz number.

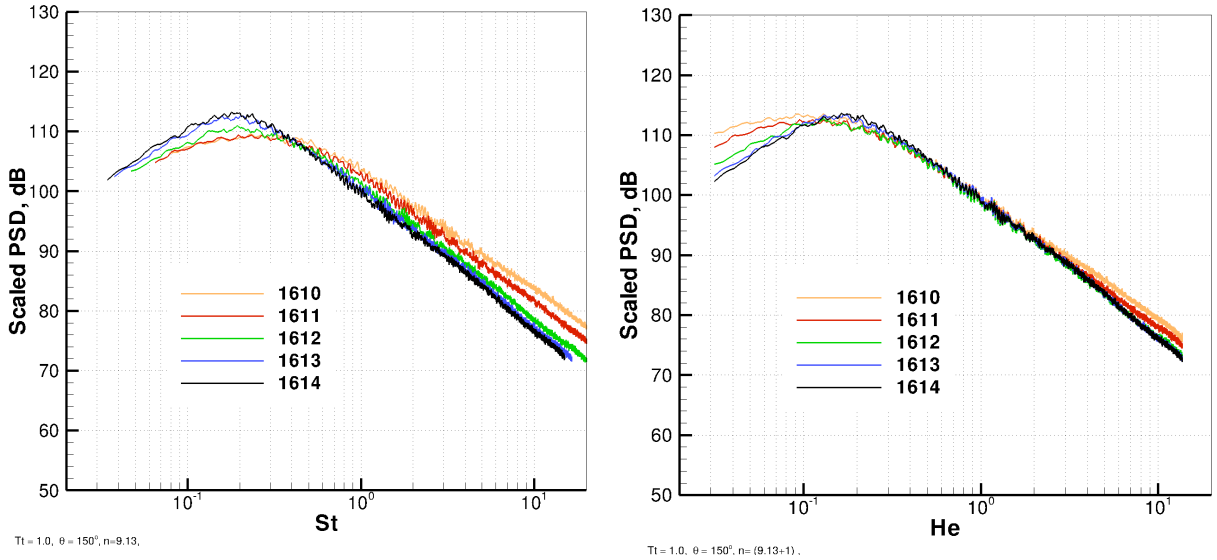

(a) (b)

Fig. 2.3 Application of power law at jet conditions of Table 2.1 ($T_t = 1.0, \theta = 150^o$)
(a) Scaled PSD per Strouhal no. (n=9.13); (b) Scaled PSD per Helmholtz no. (n=10.13)

The difference in spectral shapes at indicated set points is now clearly seen as an increase in the low frequency noise at lower jet speeds, while the spectral amplitudes at higher frequencies collapse together for all subsonic spectra.

Figure 2.4a shows a shock-free CD nozzle in addition to the subsonic spectra. The lack of collapse of the CD nozzle and subsonic noise spectra at 150^o is perhaps a good indication that a second noise component has now overwhelmed the jet mixing noise of the supersonic jets. Figure 2.4b includes two under-expanded supersonic jets (1616 and 1618) as well. As before, the supersonic noise spectra diverge substantially from the subsonic data and fail any form of a scaling law.

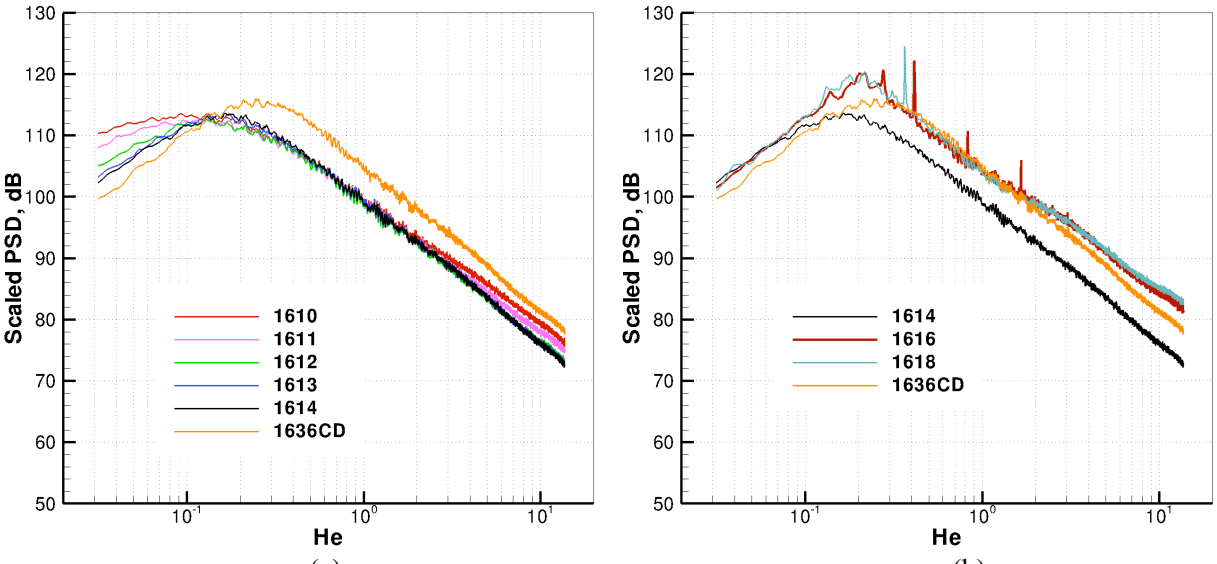

(a) (b)

Fig. 2.4 Application of power law at ($T_t = 1.0, \theta = 150^o$, n= 9.13+1). (a) smc000 at subsonic conditions and Mach 1.50 CD nozzle; (b) smc000 at both subsonic and supersonic conditions and the Mach 1.5CD nozzle – set points of Table 2.1.

2.4 Heated Jets

Jet noise spectra at three temperature ratio settings of $T_t = 1.8$, 2.2 and 2.7 are examined below. Table 2.4 shows nine nozzle conditions at a plenum temperature ratio of $T_t = 1.8$. The first seven readings represent a convergent nozzle, and consist of five subsonic jets as well as two under-expanded supersonic jets at fully expanded Mach numbers M_j of 1.24 and 1.47. Reading 1656 is due to a CD nozzle at its design pressure ratio of 2.37; and finally we have also added a reduced-screech convergent nozzle (smc021) to once again confirm the role of screech as an amplifier of the jet mixing noise.

Table 2.4 SHJAR readings at stagnation temperature ratio 1.8

Rdg	Nozzle	T_s	T_t	U_j / c_∞	M	NPR	M_j	A_j / A_e
1579	smc000	1.74	1.8	0.52	0.40	1.117	0.40	1.0
1581		1.70	1.8	0.65	0.50	1.186	0.50	1.0
1582		1.65	1.8	0.89	0.70	1.387	0.70	1.0
1583		1.55	1.8	1.12	0.90	1.692	0.90	1.0
1584		1.50	1.8	1.22	1.00	1.893	1.00	1.0
1585		1.37	1.8	1.45	1.00	2.556	1.24	1.043
1586		1.26	1.8	1.64	1.00	3.514	1.47	1.156
1656	smc014	1.40	1.8	1.40	1.18	2.378	1.18	1.0
1593	smc021	1.40	1.8	1.40	1.00	2.360	1.18	1.024

Jet noise spectra are scaled according to Eq. 2.6 and presented in Figures 2.5 through 2.7. Similar to the unheated cases, the under-expanded jets exhibit screech, which is also accompanied with an amplification of the jet mixing noise (Figs. 2.5 and 2.6). According to Fig. 2.6a, the CD nozzle is completely shock-free at 120° and provides a perfect collapse with the subsonic noise data.

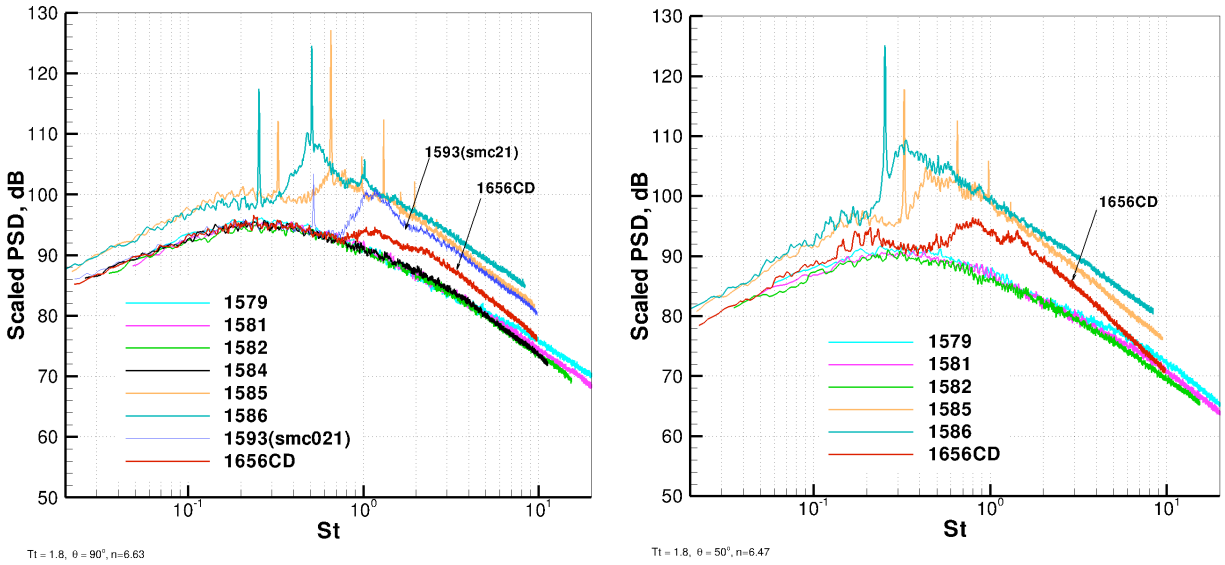

Fig. 2.5 Application of power law at conditions of Table 2.4 ($T_t = 1.8$).
(a) $\theta = 90^o$, **n= 6.63**; (b) $\theta = 50^o$, **n=6.47.**

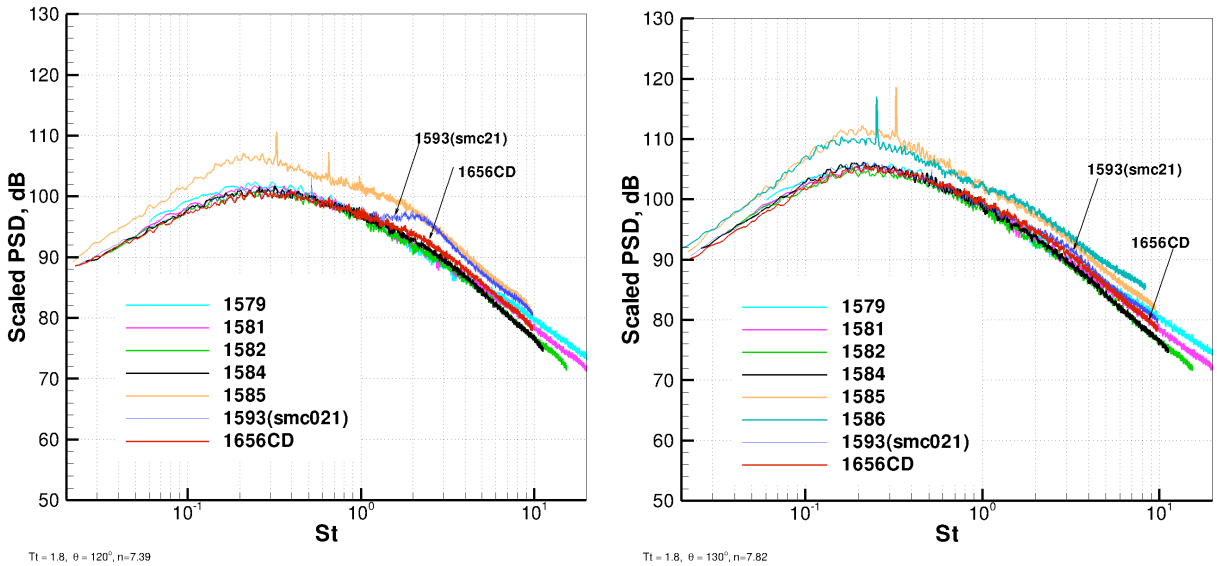

Fig. 2.6 Application of power law at conditions of Table 2.4 ($T_t = 1.8$).

(a) $\theta = 120^o$, n= 7.39; (b) $\theta = 130^o$, n=7.82.

At 130° (Fig. 2.6b) the shock-associated noise nearly disappears from both CD and reduced-screech convergent nozzle spectra. Amplification of jet mixing noise due to screech is seen as an additional 2 to 6 dB noise at under-expanded conditions of 1585 and 1586.

The aft angle spectra exhibit a broadening of the spectral peak at both low and high velocity limits. The PSD per Helmholtz number at 150° shows a perfect collapse of the high frequency roll-off at subsonic conditions with an adjusted power factor n = 8.85+1 (see Fig. 2.7a)

Jets at supersonic acoustic Mach number display a gradual broadening at their spectral peak. If we attempt to collapse all set points of Table 2.4 using a constant power factor of 9.85 at 150°, the low frequency data appear to approach a plateau, while the high frequency noise continues to increase (Fig. 2.7b). This, most probably, is indicative of a second noise component at small aft angles. A different presentation of the 150° data that attempts to collapse the high frequency roll-off is shown in Fig. 2.8. Note that this is achieved only when each jet at a supersonic acoustic Mach number is scaled with a different velocity power factor.

Examination of the spectral collapse with Helmholtz number at 160° using a constant power factor of n=9.90 is shown in Fig. 2.9. The presence of a second spectral peak at this angle under supersonic condition can be seen even more prominently relative to those at 150°.

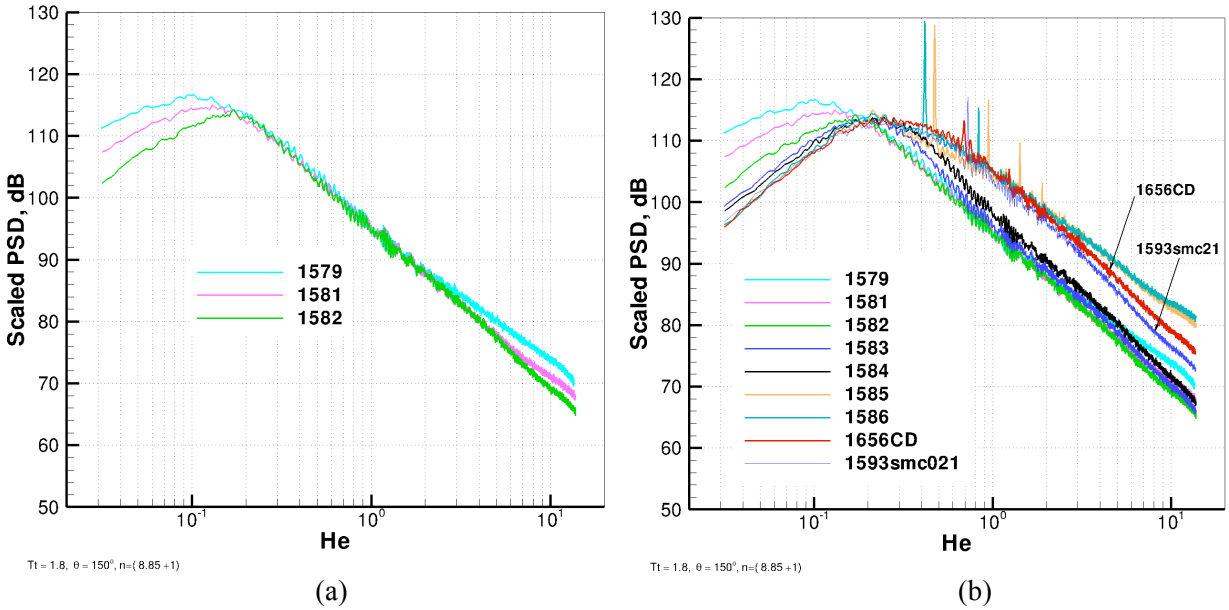

Fig. 2.7 Application of power law at conditions of Table 2.4 ($T_t = 1.8, \theta = 150^o$, n= 8.85+1). (a) Subsonic jets; (b) a mix of subsonic and supersonic jets.

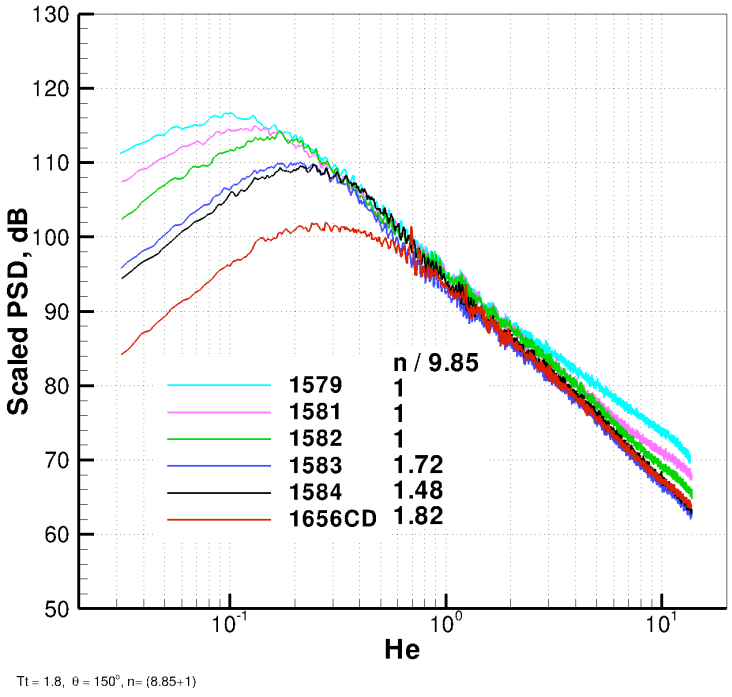

Fig. 2.8 High frequency spectral collapse at conditions of Table 2.4 with a variable velocity power factor n ($T_t = 1.8, \theta = 150^o$).

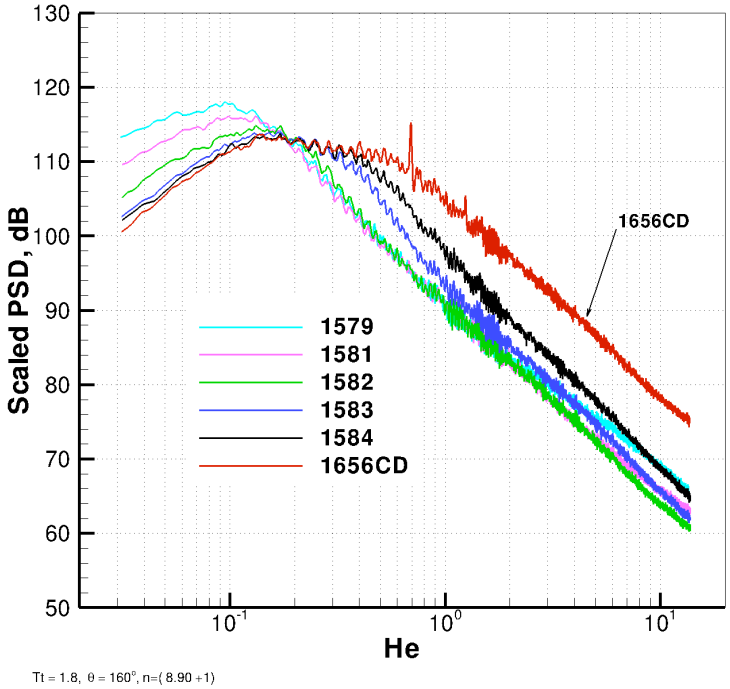

Fig. 2.9 Application of power law at conditions of Table 2.4 ($T_t = 1.8, \theta = 160^o$, n= 8.90+1).

For completeness, jet noise spectra at higher plenum temperatures of 2.2 and 2.7 (Tables 2.5 and 2.6) are also shown in figures 2.10 and 2.11. Each Table consists of a convergent nozzle smc000 at five subsonic conditions as well as two under-expanded supersonic conditions. The collapse of the spectral data (shown at 50, 90, 120, 150 and 160 degrees) is in general agreement with the trends discussed earlier at temperatures T_t = 1.0 and 1.8. The aft angle spectra demonstrate a clear broadening at the peak with increasing jet speed. This is also accompanied with a departure from the high-frequency amplitude roll-off observed in subsonic data.

Table 2.5 SHJAR readings at stagnation temperature ratio 2.20

Rdg	Nozzle	T_s	T_t	U_j / c_∞	M	NPR	M_j	A_j / A_e
1568	smc000	2.13	2.20	0.58	0.40	1.117	0.40	1.0
1569		2.10	2.20	0.72	0.50	1.186	0.50	1.0
1570		2.00	2.20	0.99	0.70	1.387	0.70	1.0
1571		1.91	2.20	1.24	0.90	1.692	0.90	1.0
1572		1.83	2.20	1.35	1.00	1.893	1.00	1.0
1574		1.69	2.20	1.61	1.00	2.556	1.24	1.043
1577		1.54	2.20	1.82	1.00	3.514	1.47	1.156

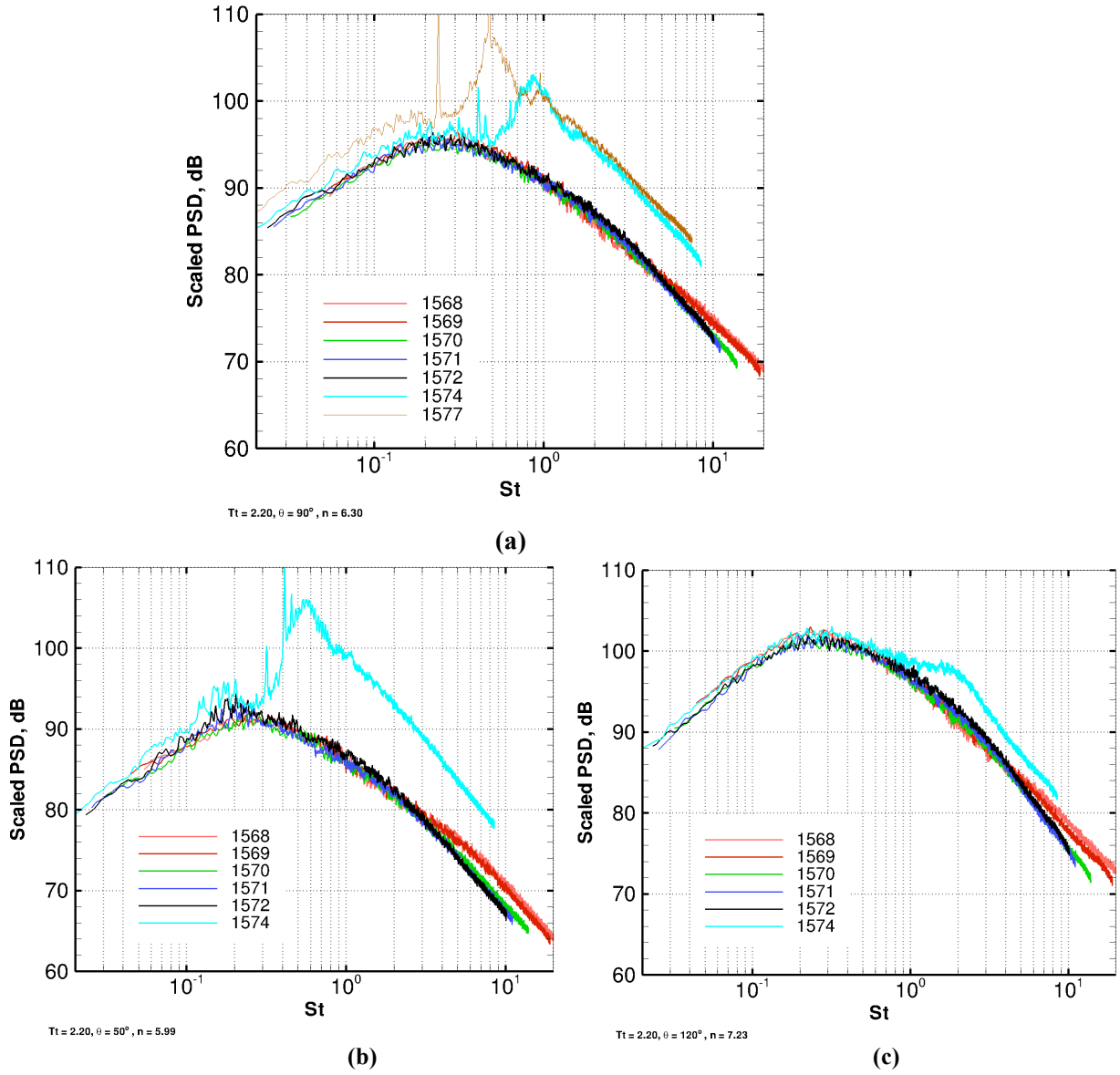

Fig. 2.10 Application of power law at jet conditions of Table 2.5 at T_t=2.20.
(a) $\theta = 90^o$, n= 6.30; (b) $\theta = 50^o$, n= 5.99; (c) $\theta = 120^o$, n=7.23

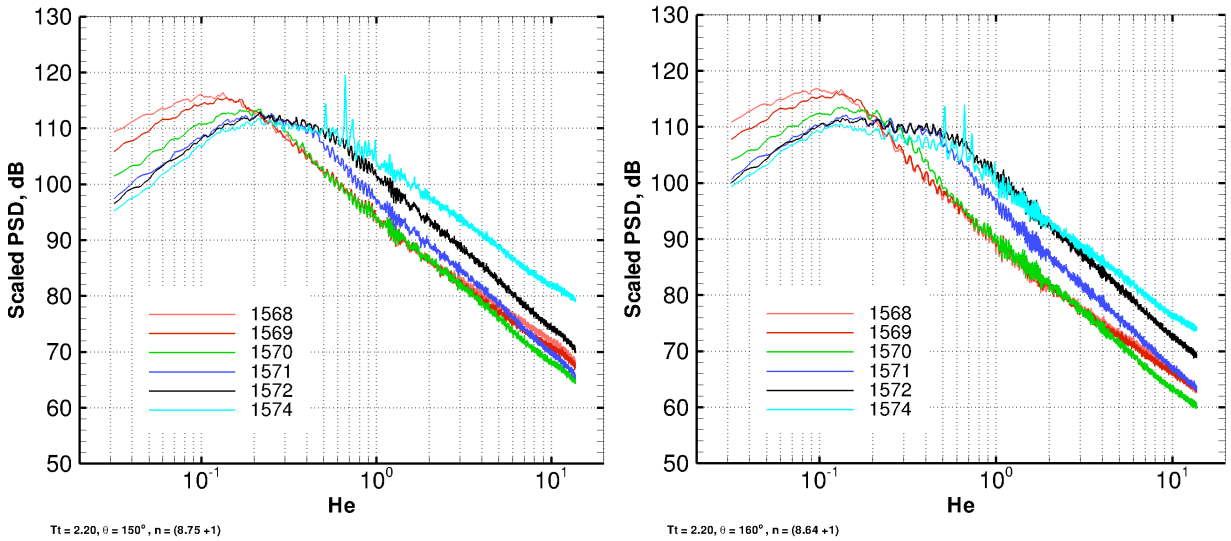

(d) **(e)**

Fig. 2.10 (cont'd) Application of power law at jet conditions of Table 2.5 at T_t=2.20.

(d) $\theta = 150^o$, n=9.75; (e) $\theta = 160^o$, n=9.64.

Table 2.6 SHJAR readings at stagnation temperature ratio 2.70

Rdg	Nozzle	T_s	T_t	U_j / c_∞	M	NPR	M_j	A_j / A_e
1561	smc000	2.62	2.70	0.64	0.40	1.117	0.40	1.0
1562		2.58	2.70	0.80	0.50	1.186	0.50	1.0
1563		2.47	2.70	1.09	0.70	1.387	0.70	1.0
1564		2.35	2.70	1.37	0.90	1.692	0.90	1.0
1565		2.26	2.70	1.50	1.00	1.893	1.00	1.0
1566		2.07	2.70	1.79	1.00	2.556	1.24	1.043
1567		1.90	2.70	2.01	1.00	3.514	1.47	1.156

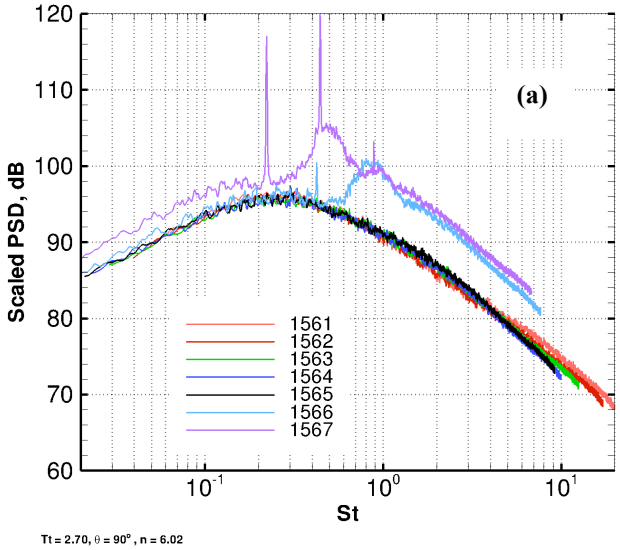

Fig. 2.11 Application of power law at jet conditions of Table 2.5 at T_t=2.70.

(a) $\theta = 90^o$, n= 6.02.

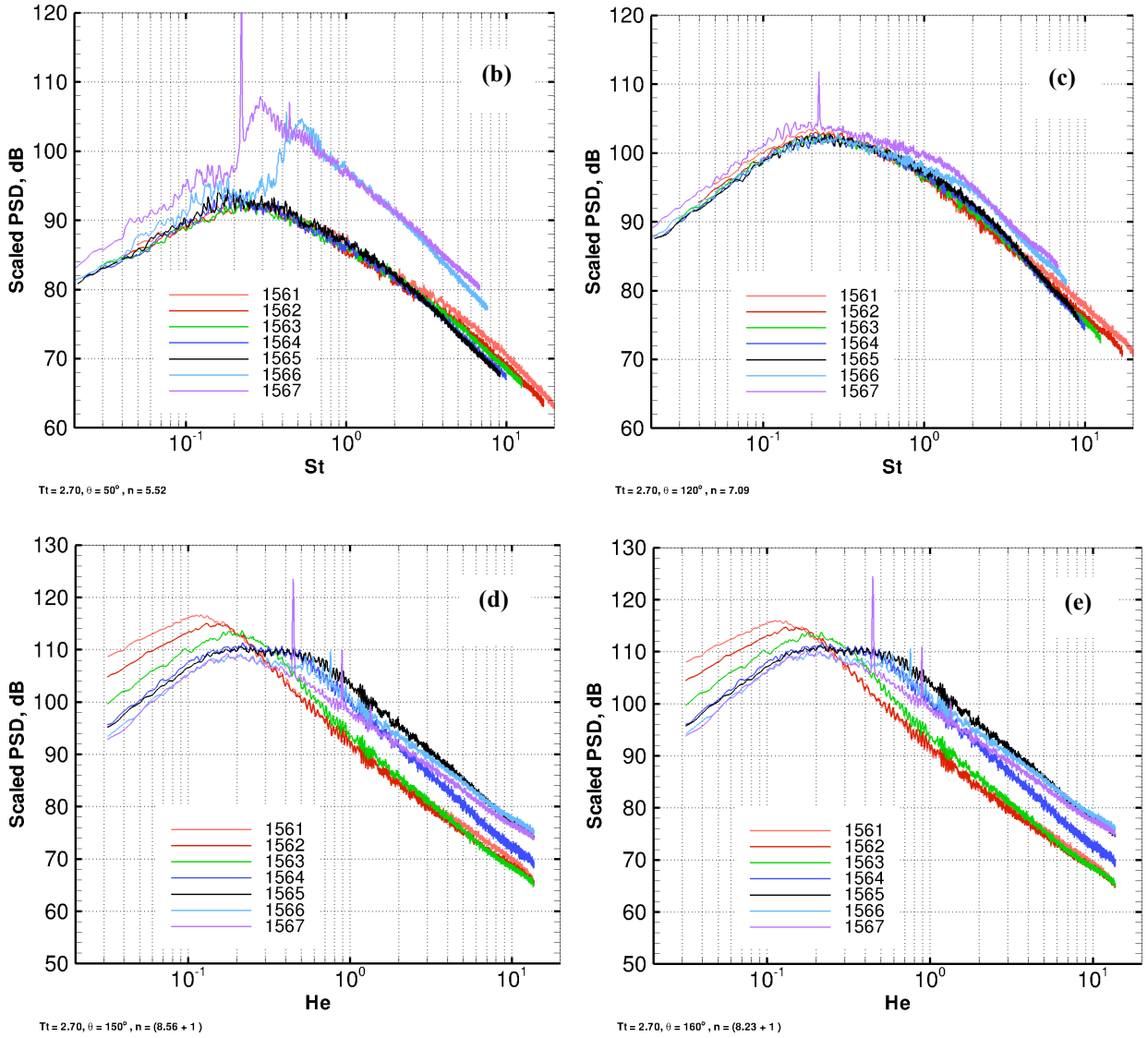

Fig. 2.11 (cont'd) Application of power law at jet conditions of Table 2.5 at T_t=2.70.

(b) $\theta = 50^o$, **n= 5.52; (c)** $\theta = 120^o$, **n=7.09;**

(d) $\theta = 150^o$, **n=9.56; (e)** $\theta = 160^o$, **n=9.23.**

2.5 Examination of Data at Constant Static Temperature

Spectral data collapse at three temperature setting of T_s = 1.0, 1.76 and 2.0 are illustrated using the velocity power factor of Fig. 1.13 (raw data for the regression parameters n and B at a constant static temperature are also provided in Tables 2.8 and 2.9 below).

Table 2.7 shows operating conditions for 11 jets at a constant static temperature ratio of 1.0. The first three configurations are subsonic jets. The next four jets, identified as smc021, are reduced-screech convergent nozzles at under-expanded conditions. These jets display strong shock noise at mid- to high frequency. The last four readings are CD nozzles operating at their respective design points, i.e. at fully expanded Mach numbers of 1.18, 1.40, 1.50 and 1.80 respectively. In practice, the CD nozzle spectra are not completely shock-free.

Table 2.7 SHJAR readings at static temperature ratio 1.0

Rdg	Nozzle	T_s	T_t	U_j / c_∞	M	NPR	M_j	A_j / A_e
1521	smc000	1.0	1.04	0.50	0.50	1.18	0.50	1.0
1523		1.0	1.10	0.70	0.70	1.38	0.70	1.0
1524		1.0	1.16	0.90	0.90	1.69	0.90	1.0
1587	smc021	1.0	1.28	1.18	1.0	2.37	1.18	1.024
1588		1.0	1.39	1.40	1.0	3.18	1.40	1.114
1589		1.0	1.45	1.50	1.0	3.65	1.50	1.176
1590		1.0	1.64	1.80	1.0	5.74	1.80	1.439
1655	smc014	1.0	1.28	1.18	1.18	2.38	1.18	1.0
1660	smc015	1.0	1.39	1.40	1.40	3.19	1.40	1.0
1646	smc016	1.0	1.45	1.50	1.50	3.65	1.50	1.0
1651	smc018	1.0	1.65	1.80	1.80	5.76	1.80	1.0

Table 2.8 Velocity power factor $n(\theta, T_s)$ at constant static temperature

θ^o	T_s =1.0	1.20	1.43	1.76	2.27	2.70
50	7.59	7.35	6.22	5.81	5.32	4.92
55	7.54	7.29	6.20	5.77	5.27	4.87
60	7.55	7.30	6.21	5.80	5.30	4.89
65	7.52	7.29	6.23	5.84	5.34	4.95
70	7.53	7.33	6.27	5.89	5.40	5.02
75	7.51	7.34	6.30	5.94	5.47	5.09
80	7.45	7.31	6.29	5.95	5.51	5.12
85	7.51	7.37	6.37	6.05	5.63	5.26
90	7.57	7.42	6.47	6.15	5.76	5.37
95	7.62	7.47	6.54	6.26	5.87	5.49
100	7.72	7.58	6.64	6.39	6.01	5.62
105	7.84	7.68	6.76	6.53	6.14	5.76
110	7.95	7.79	6.83	6.61	6.22	5.84
115	8.06	7.90	6.93	6.74	6.35	5.95
120	8.21	8.07	7.13	6.92	6.56	6.15
125	8.38	8.21	7.27	7.05	6.72	6.33
130	8.56	8.36	7.43	7.22	6.94	6.58
135	8.70	8.50	7.63	7.47	7.23	6.87
140	8.87	8.64	7.84	7.71	7.48	7.07
145	9.06	8.82	8.07	7.94	7.65	7.18
150	9.27	8.99	8.27	8.09	7.71	7.17
155	9.47	9.10	8.36	8.11	7.63	7.06
160	9.57	9.12	8.34	8.02	7.46	6.87
165	9.49	8.95	8.15	7.71	7.06	6.42

Table 2.9 Intercept parameter $B(\theta, T_s)$ at constant static temperature

θ^o	$T_s = 1.0$	1.20	1.43	1.76	2.27	2.70
50	94.54	92.80	92.03	91.71	91.85	92.29
55	94.75	93.00	92.33	92.09	92.21	92.65
60	95.15	93.46	92.25	92.10	92.18	92.56
65	95.40	93.84	93.07	92.92	92.94	93.35
70	95.75	94.29	93.38	93.23	93.24	93.66
75	96.16	94.81	94.23	94.11	94.10	94.49
80	96.37	95.16	94.57	94.50	94.55	94.90
85	97.05	95.92	95.44	95.37	95.40	95.71
90	97.77	96.72	96.63	96.58	96.59	96.85
95	98.29	97.34	97.11	97.12	97.11	97.41
100	99.03	98.16	98.08	98.17	98.15	98.44
105	99.82	99.01	99.17	99.28	99.23	99.58
110	100.52	99.79	99.76	99.93	99.87	100.22
115	101.26	100.66	100.64	100.90	100.87	101.24
120	102.20	101.71	101.93	102.18	102.20	102.54
125	103.34	102.91	103.12	103.39	103.50	103.93
130	104.47	104.06	104.33	104.66	104.90	105.42
135	105.26	104.89	105.48	105.93	106.24	106.78
140	106.27	105.92	106.58	107.14	107.45	107.92
145	107.30	106.99	107.82	108.34	108.47	108.78
150	108.20	107.84	108.72	109.07	108.89	109.02
155	108.84	108.35	109.17	109.25	108.74	108.72
160	109.06	108.34	109.03	108.82	107.97	107.82
165	108.07	107.09	107.92	107.25	105.89	105.53

Figure 2.12a shows data collapse at 90° for all seven convergent nozzles listed in Table 2.7. Spectral collapse at St < 0.20 is an indication that the smc021nozzle has successfully eliminated the screech-related mixing noise amplifications at supersonic speed. According to Fig. 2.12b, the CD nozzle spectra conform to the power law as well, although shock related noise appears to contaminate the spectra at $St >$ 0.40. The shock-associated noise gets relatively stronger at forward angles (Fig 2.13a), and covers a wider frequency range. At 90°, shock noise is totally absent in all 9 jets at $St < 0.20$ as seen in Figs. 12a and b.

Data collapse at 150° is presented as a function of Helmholtz number and with an adjusted velocity power factor of n+1 as noted in Eq. 2.7 (see Fig. 2.13b). The roll-off of the high frequency amplitude is seen to follow the power law as long as the acoustic Mach number remains subsonic. Once U_j/c_∞ exceeds 1.0, the low frequency segment of the spectra reach a limit, while the high-frequency noise tends to increase. As before, we attribute this additional high frequency noise to a different source component that is radiating at shallow angles. The pattern gets considerably irregular when supersonic CD nozzles are also added to the group (Fig. 2.14a). Changing the abscissa to the Strouhal number provides some semblance at low frequency (Fig. 2.14b), however, as we saw in Fig. 2.8, supersonic jets do not obey a constant power factor law.

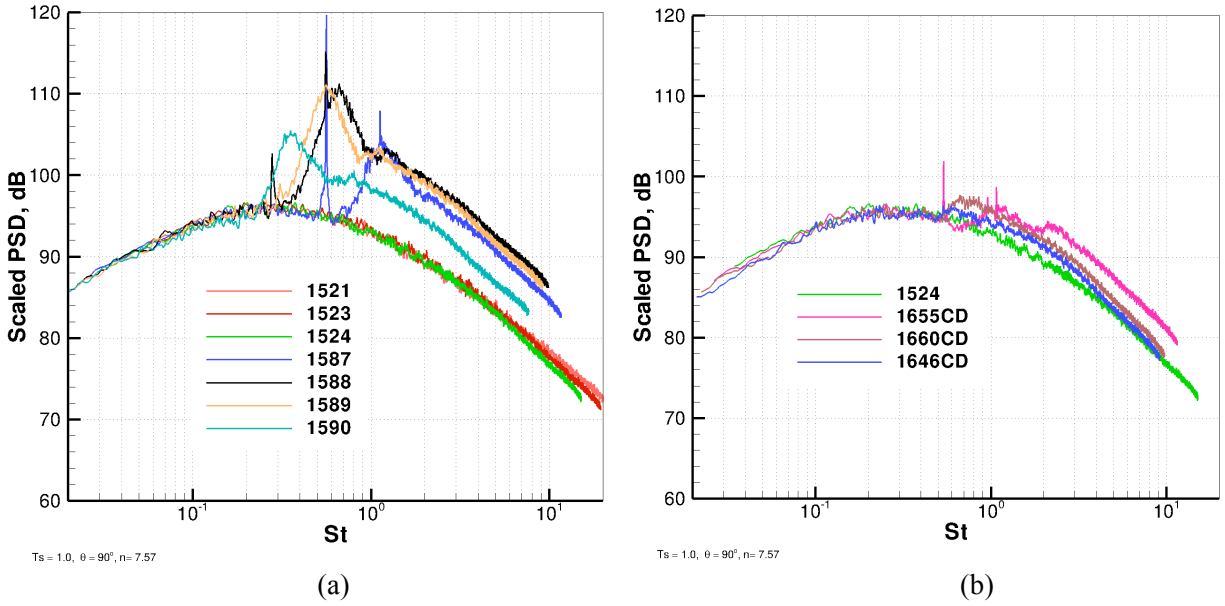

Fig. 2.12 Application of power law at nozzle conditions of Table 2.7 ($T_s = 1.0, \theta = 90^o$, n= 7.57). (a) Convergent nozzles; (b) A base convergent nozzle (smc000) and three CD nozzles.

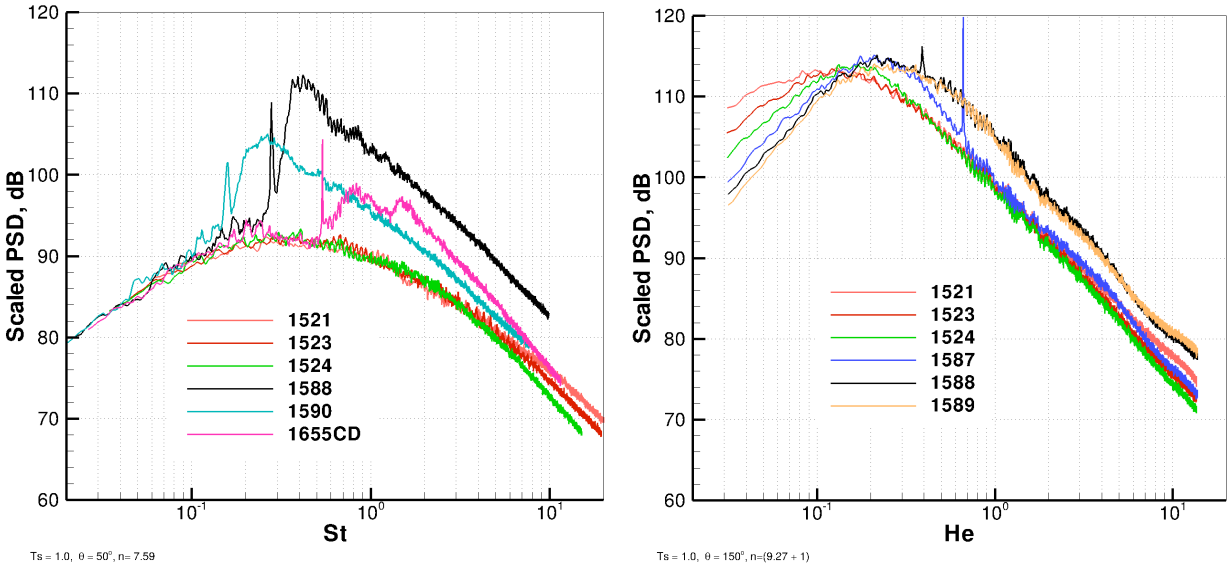

Fig. 2.13 Application of power law at nozzle conditions of Table 2.7 (T_s = 1.0).
(a) $\theta = 50^o$, n= 7.59; (b) $\theta = 150^o$, n=10.27.

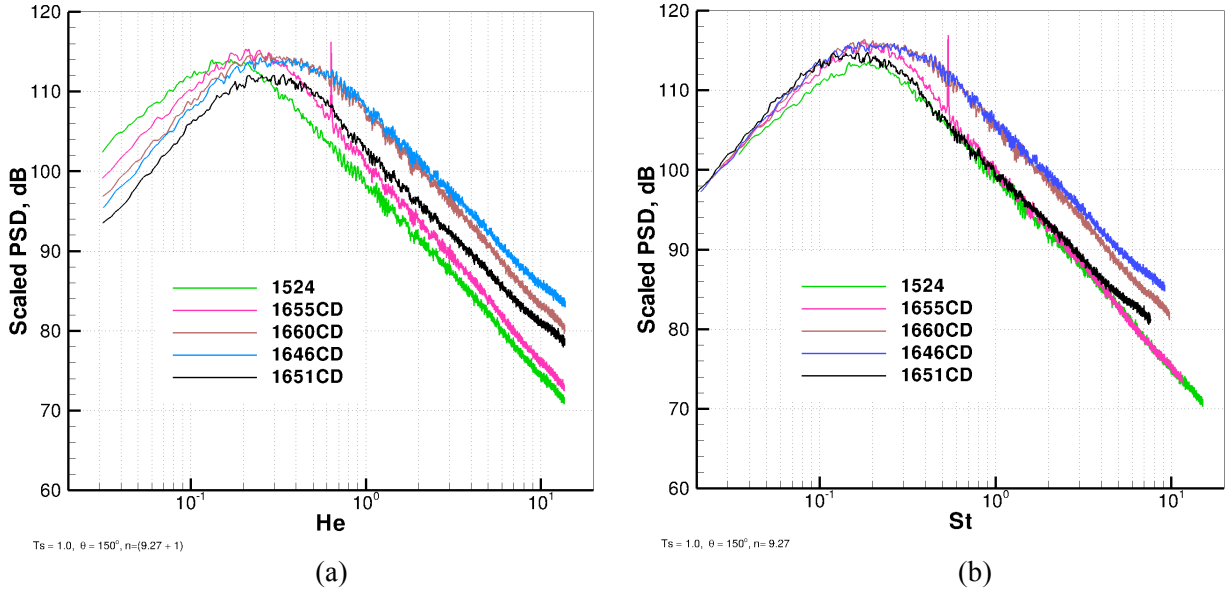

Fig. 2.14 Application of power law in CD nozzles at conditions of Table 2.7 ($T_s = 1.0, \theta = 150^o$)
(a) PSD per Helmholtz no. , n= 10.27; (b) PSD per Strouhal no. n=9.27.

The application of the velocity power law at T_s = 1.76 using eight shock-free subsonic conditions of Table 2.10 is examined in Figs 2.15 and 2.16.

Table 2.10 SHJAR readings at static temperature ratio 1.76

Rdg	Nozzle	T_s	T_t	U_j / c_∞	M	NPR	M_j	A_j / A_e
5615	smc000	1.76	1.79	0.39	0.29	1.06	0.29	1.0
5578		1.76	1.81	0.49	0.37	1.10	0.37	1.0
5614		1.76	1.83	0.59	0.45	1.14	0.45	1.0
5613		1.76	1.86	0.69	0.52	1.20	0.52	1.0
5612		1.76	1.89	0.79	0.60	1.27	0.60	1.0
5579		1.76	1.92	0.89	0.67	1.35	0.67	1.0
5629		1.76	2.04	1.18	0.89	1.67	0.89	1.0
5580		1.76	2.11	1.32	1.0	1.89	1.0	1.0

A nearly perfect collapse of data at typical sideline angles of 50° and 90° is seen in Figs. 2.15a and 2.15b. At an aft-angle of 150°, the power law was examined using both frequency parameters. A Strouhal scaling is much less successful as seen in Fig. 2.16a. On the other hand, Fig. 2.16b shows a collapse of the amplitudes in the high-frequency roll-off with respect to the Helmholtz number as long as the acoustic Mach number remains subsonic. The figure also demonstrates that the low frequency segment of the spectra becomes relatively less peaky at low speeds ($U_j/c_\infty < 0.50$), however a clear peak develops at higher speeds near He = 0.15. According to Fig. 2.16b, at supersonic speeds (i.e. readings 5629 and 5580) the low frequency noise tends to approach a limit while the high frequency noise diverges from the subsonic spectra at mid to high frequency.

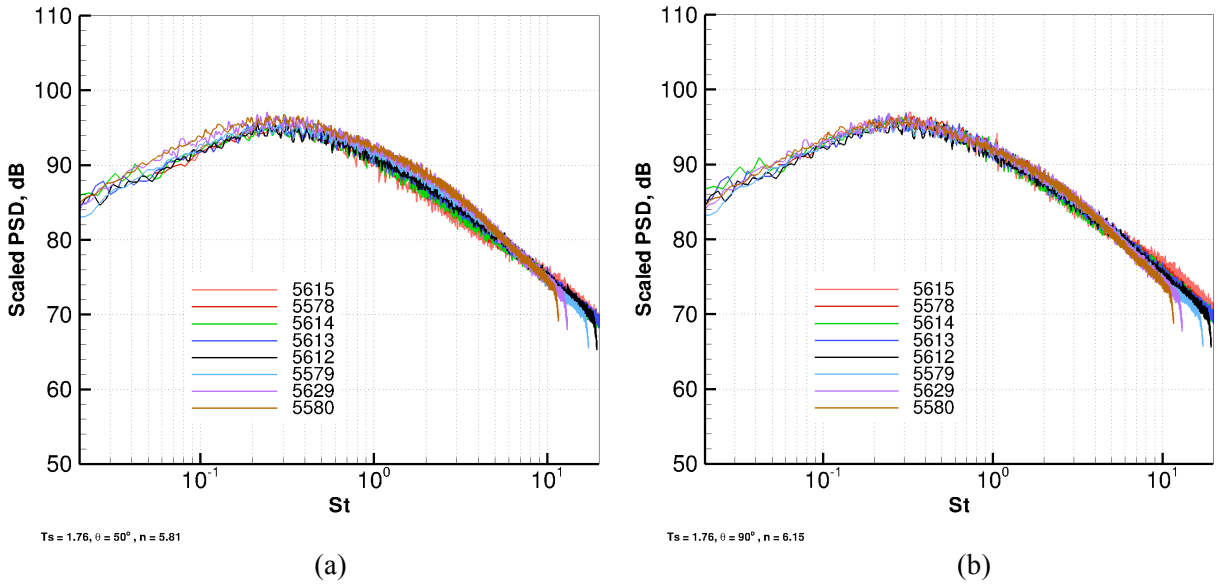

Fig. 2.15 Application of power law at conditions of Table 2.10 (T_s = 1.76).
(a): $\theta = 50^o$, n= 5.81; (b) $\theta = 90^o$, n=6.15.

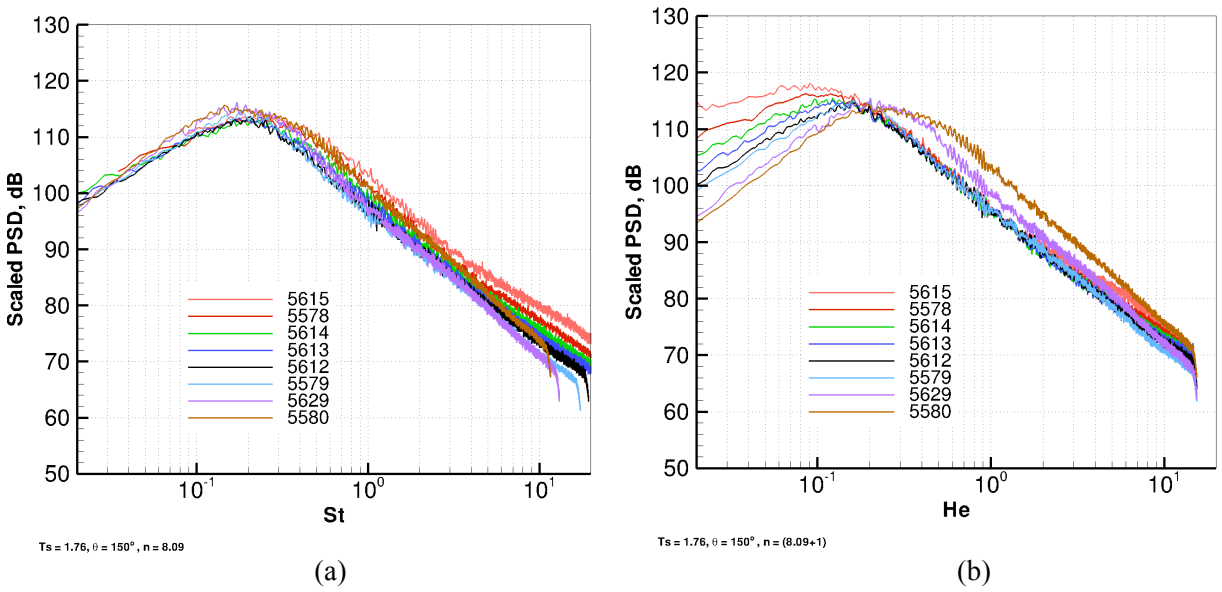

Fig. 2.16 Application of power law at conditions of Table 2.10 ($T_s = 1.76, \theta = 150^o$) (a): PSD per Strouhal no., n= 8.09; (b) PSD per Helmholtz no. , n=9.09.

And finally, the application of the velocity power law at the next static temperature ratio of $T_s = 2.70$ is examined at subsonic conditions of Table 2.11.

Table 2.11 SHJAR readings at static temperature ratio 2.70

Rdg	Nozzle	T_s	T_t	U_j / c_∞	M	NPR	M_j	A_j / A_e
5585	smc000	2.70	2.73	0.39	0.24	1.04	0.24	1.0
5586		2.70	2.77	0.59	0.36	1.09	0.36	1.0
5587		2.70	2.80	0.69	0.42	1.12	0.42	1.0
5588		2.70	2.81	0.79	0.48	1.17	0.48	1.0
5590		2.70	2.97	1.17	0.72	1.40	0.72	1.0
5592		2.70	3.03	1.32	0.81	1.52	0.81	1.0
5581		2.70	3.09	1.47	0.91	1.69	0.91	1.0

Figures 2.17a and 2.17b illustrate the collapse of data at 50° and 90° respectively. According to Fig. 2.17c, aft-angle data fail the power law when Strouhal frequency parameter is selected. On the other hand, an excellent collapse of the amplitudes in the high-frequency spectral roll-off is seen vs. the Helmholtz number provided that the acoustic Mach number remains subsonic (see Figs. 2.18a and 2.18b at 150° and 160° respectively). As before, the supersonic jets tend to diverge from the subsonic cases at mid to high frequency.

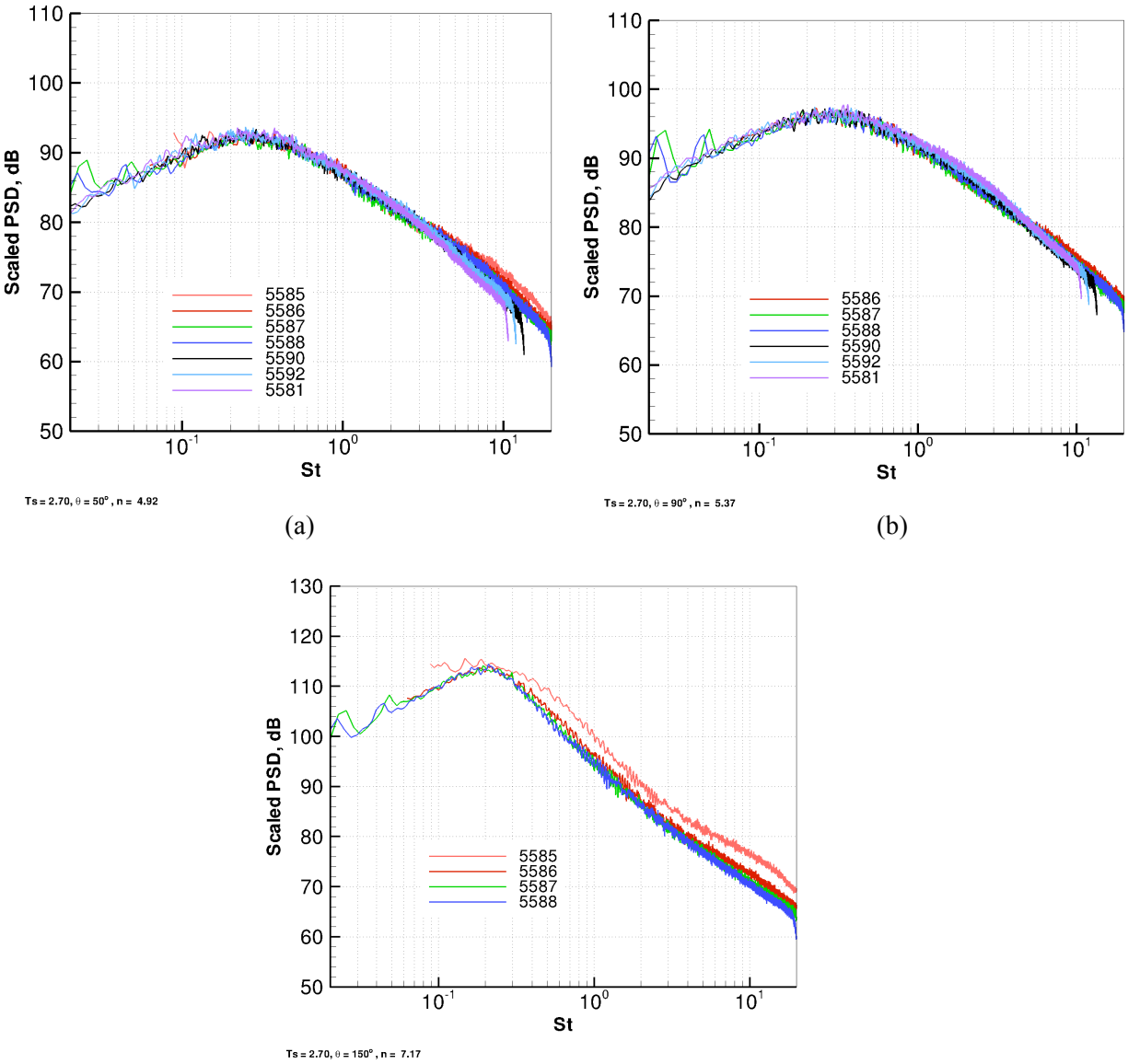

Fig. 2.17 Application of power law at conditions of Table 2.11 (T_s =2.70).
(a) $\theta = 50^o$, n= 4.92; (b) $\theta = 90^o$, n=5.37; (c) $\theta = 150^o$, n= 7.17.

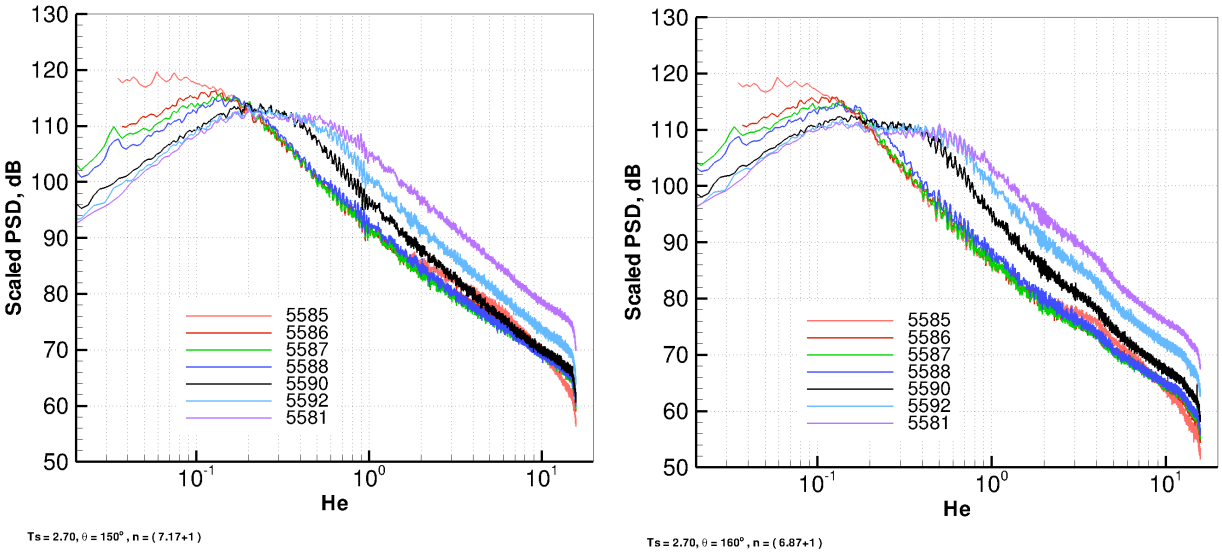

(a) (b)

Fig. 2.18 Application of power law at conditions of Table 2.11 (T_s=2.70). (a) $\theta = 150^o$, n=8.17; (b) $\theta = 160^o$, n=7.87.

2.6 Examination of the Power Law Across Temperatures

The application of velocity power law across various jet temperatures requires two parameters n and B. Velocity scaling is achieved when the difference in intercept parameters B at the two temperatures is added to the scaling formula 2.6

$$scaled\ PSD = PSD - 10n(\theta,T)Log(U_j / c_\infty) - 10Log(A_j / A_e) + \left(B_0(\theta,T) - B(\theta,T)\right) \qquad (2.8)$$

B_0 is the intercepts parameter for a jet that is considered as the datum. As an example consider a set of subsonic heated jets (i.e. base smc000 nozzle) at shock-free conditions of Table 2.12 (these jets were also listed in Table 1.2). Note that ratio of the fully expanded jet area to the exit area is $A_j / A_e = 1.0$ for all jets. Parameters $n(\theta,T)$ and $B(\theta,T)$ at each static temperature of interest are listed in Tables 2.8 and 2.9.

Table 2.12 Selected SHJAR readings across different temperatures

Rdg	T_s	T_t	U_j/c_∞	M	NPR	$\mathrm{Re}\times 10^{-5}$
1524	1.0	1.16	0.90	0.90	1.69	10.60
1530	1.20	1.36	0.90	0.82	1.563	7.69
5624	1.43	1.59	0.89	0.75	1.451	5.62
5629	1.76	2.04	1.18	0.89	1.667	5.20
5605	2.27	2.42	0.89	0.59	1.264	2.58

Figure 2.19 show the results when reading 1524 (i.e. T_s=1) is selected as the datum temperature. Note that the acoustic Mach number is of the order of ~0.90 in four jets within this group. The differences in

the attenuation of the high frequency noise at 150° (Fig. 2.19d) may be attributed to the temperature-related refraction effect.

As a note, spectral data presented in [Ref. 18] display the presence of a second peak at low frequency (at a lower frequency than the main peak shown here) with increasing jet temperature, and an explanation is given in terms of the Reynolds number effect. In [Ref. 18] it is argued that jets at Reynolds number less than ~400,000 display a second low frequency peak with increasing jet temperature. The highest temperature jet in our group as seen in Table 2.12 (i.e. reading 5605) has a Reynolds number of 2.58 x10^5, which is well below the threshold number quoted above, and yet there is no evidence of an additional low frequency "hump" at any of the four angles shown here. It is speculated that the extra low frequency noise reported in [Ref. 18] is likely facility related, and not an element of the jet noise.

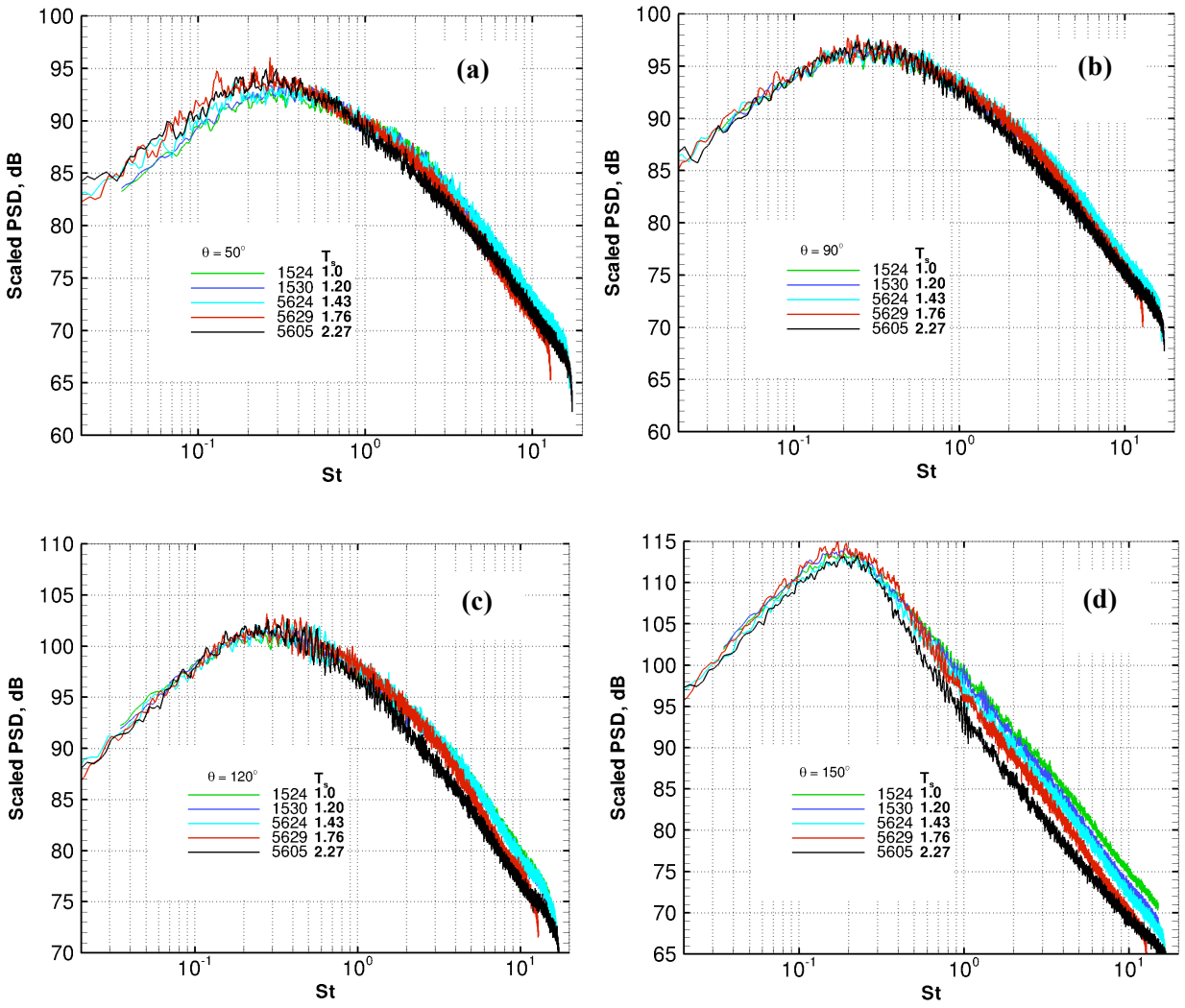

Fig. 2.19 Application of power law across temperatures at nozzle conditions of Table 2.12. (a) 50° ; (b) 90°; (c) 120° ; (d) 150°.

To further shed light on the effect of heat addition on jet noise, spectra from a set of low Mach number readings of Table 2.13 are examined following the scaling equation 2.8 and combined with n and B parameters as listed in Tables 2.8 and 2.9. Note that $U_j/c_\infty \le 0.50$ at all six conditions. Figure 2.20 shows that heat addition increases the low frequency noise in such low speed jets at all angles (note that four jets are at a constant acoustic Mach number of 0.39). In the example following Table 2.12, we

demonstrated that heat addition lacks a similar effect at the acoustic Mach number of 0.90 regardless of the Reynolds number.

Additionally, Fig. 2.20 also point to the presence of the facility-related noise at very low frequency. The advantage of displaying jet noise spectra in a narrow band is that such extraneous noise components are easy to discern. If presented in a third-Octave band, it might incorrectly be construed as a second peak at low frequency. Measurements of [Ref. 18] provide a different explanation, and conclude that heat addition has a more pronounced effect on low frequency noise at D=1.50 in., and the effects disappear completely at D =2.45 in.

Table 2.13 Selected SHJAR readings at low Mach number – different temperatures

Rdg	T_s	T_t	U_j/c_∞	M	NPR	$\mathrm{Re}\times 10^{-5}$
1521	1.0	1.04	0.50	0.50	1.180	5.89
1528	1.20	1.25	0.50	0.45	1.153	4.27
5619	1.43	1.45	0.39	0.33	1.078	2.46
5615	1.76	1.79	0.39	0.29	1.060	1.73
5599	2.27	2.30	0.39	0.26	1.040	1.13
5585	2.70	2.73	0.39	0.24	1.040	0.85

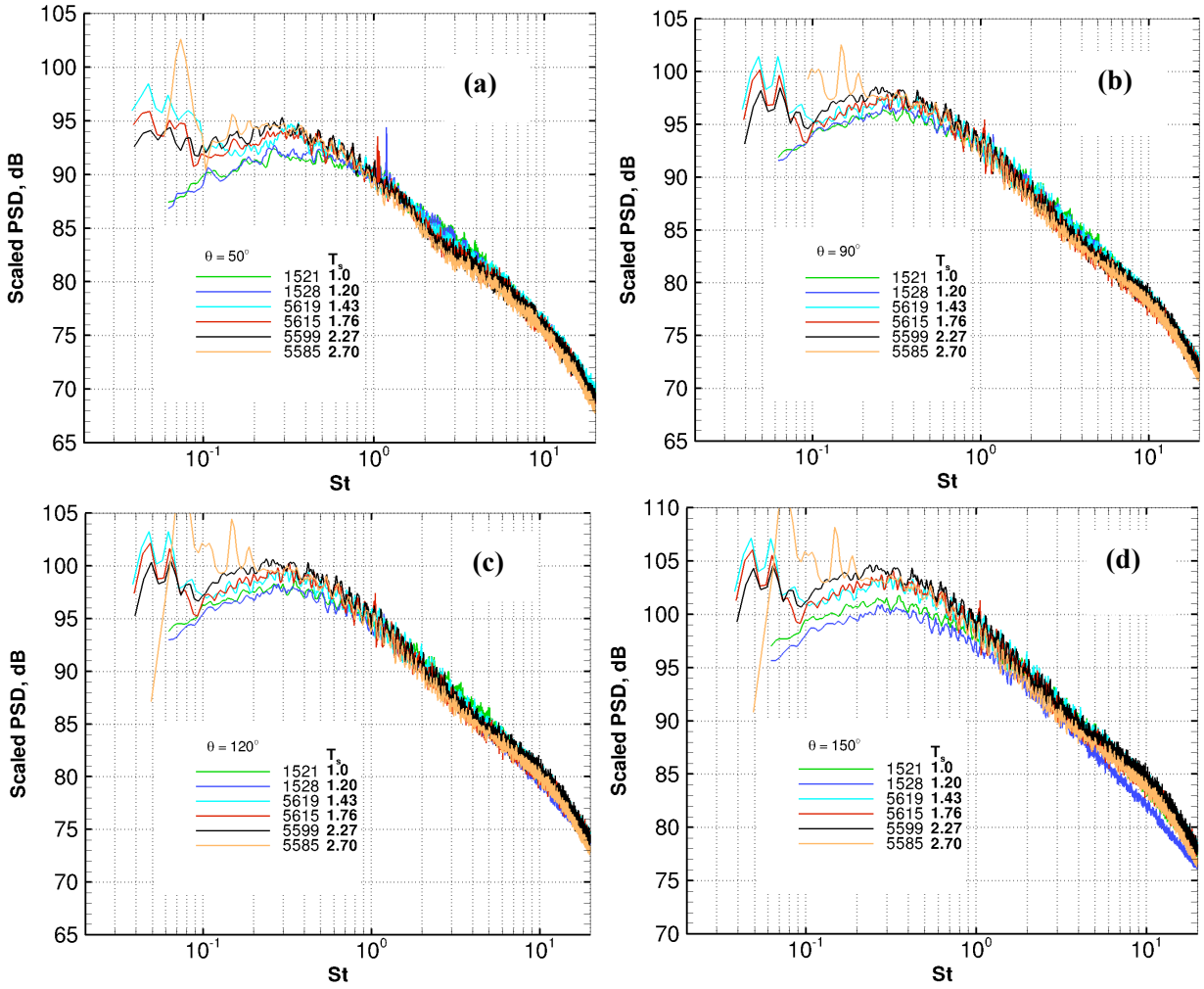

Fig. 2.20 Application of power law across temperatures at jet conditions of Table 2.13 (a) 50° ; (b) 90° ; (c) 120° ; (d) 150°.

As a final example in this section, scaling Eq. 2.8 is tested across different stagnation temperatures. Table 2.14 shows four shock-free Mach 1.0 jets (i.e. $A_j / A_e = 1.0$). Required regression parameters n and B are listed in Tables 2.2 and 2.3. We also choose reading 1614 as the datum temperature. Generally speaking, the three heated jets appear to conform to the power law along sideline angles as seen in Fig. 2.21. The unheated jet (i.e. smc000-1614) displays a distinctly different spectral shape at all angles. At an aft angle of 150°, the application of the power law is relatively more successful at low frequency. The lack of collapse of the high frequency noise at 150° may be attributed to a combined refraction effect (due to temperature differences), as well increasing presence of a second noise component at supersonic speeds.

Table 2.14 SHJAR readings across different stagnation temperatures

Rdg	Nozzle	T_t	U_j / c_∞	M	NPR	$\mathrm{Re}\times 10^5$
1614	smc000	1.0	0.91	1.0	1.89	10.73
1584		1.8	1.22	1.0	1.89	7.19
1572		2.2	1.35	1.0	1.89	5.68
1565		2.7	1.50	1.0	1.89	4.47

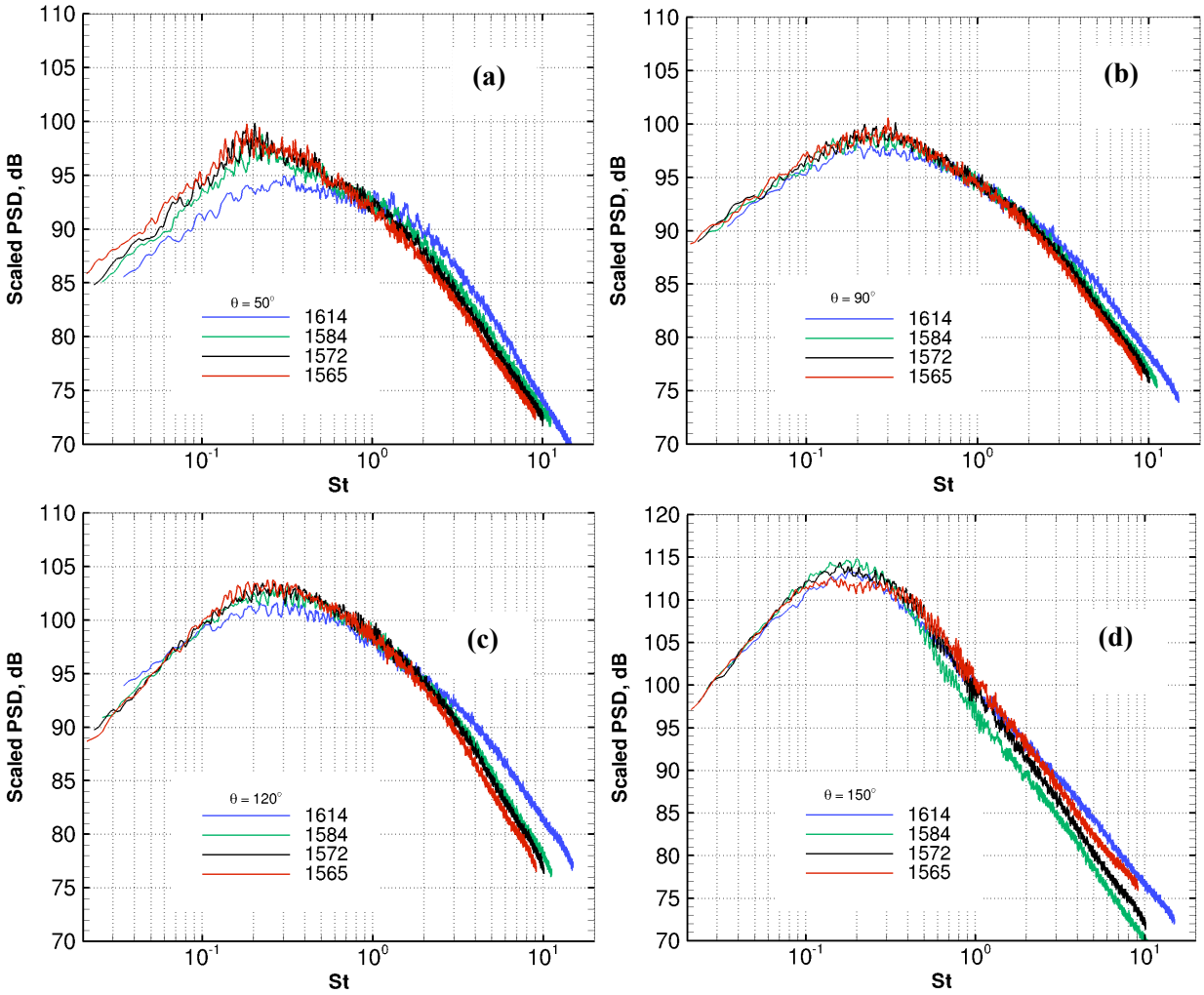

Fig. 2.21 Application of power law across temperatures at jet conditions of Table 2.14 (a) 50° ; (b) 90° ; (c) 120° ; (d) 150°.

3.1 Noise Components

A typical jet noise spectrum, in general, consists of three distinct components, i.e. jet mixing noise, shock-associated noise, and screech. Shock noise is broadband, relatively stronger at forward angles, and is present when a nozzle is operated at under- or over- expanded conditions [Refs. 19-21]. Harper-Bourne and Fisher [Ref. 22] pioneered a formalism that estimates the shock noise component of supersonic jets. Screech noise, on the other hand, appears as isolated spikes at almost all angles in imperfectly expanded jets. When screech tones are strong enough, they may excite the jet by transferring energy to the large structures of the flow. The result is an amplification of the broadband mixing noise (AMN). For example, Fig. 2.5 shows that jet mixing noise in an under-expanded convergent nozzle smc000 (at readings 1585 and 1586) could be amplified anywhere from 4 to 6 dB due to screech tones. The same figure shows that, when the nozzle lip is modified with fine notches that reduce screech (configuration smc021), the AMN noise disappears completely, and subsequently mixing noise conforms to the power law.

The amplification of the broadband jet noise by pure tone has been shown experimentally [Ref. 5]. In many cases, reducing the fluctuating radial velocity near the nozzle lip may control the amplification. For example, an acoustic lining such as a porous tailpipe at the nozzle exit succeeds in creating a continuous transition between two regions, prior to and after the exit, thus reducing the amplification.

In this section, we use the velocity power law to identify the jet mixing noise and shock-associated noise. It is shown that the scaling laws help identify the amplification. Since the AMN noise is a by-product of screech, which in turn is associated with the shock noise, we consider any such amplification as part of the shock noise rather than a separate entity.

A systematic approach to the problem of identifying noise components is presented in the following order:

1) An under-expanded convergent nozzle excluding amplification
2) Under-expanded convergent nozzle with screech (and AMN noise)
3) Under-expanded convergent-divergent (CD) nozzles.

Within the first category a reduced-screech convergent nozzle at a pressure ratio larger than 1.89 would be appropriate. For this example, we discuss configuration smc021-1605 from Table 2.1 at *NPR*=2.32. To isolate the mixing noise component in this under-expanded jet, we may apply velocity power scaling to any one of the subsonic jets listed in Table 2.1 (i.e. at T_t=1.0), and scale that to a fully expanded jet velocity at configuration smc021-1605. Since the exit area A_e for all SHJAR nozzles are identical, the scaling law applies as

$$PSD_2 = PSD_1 + 10n(\theta,T)Log(U_{j2}/U_{j1}) + 10Log(A_{j2}/A_{j1}). \qquad (3.1)$$

Subscripts 1 and 2 refer to lower-speed (i.e. datum) and higher-speed (i.e. destination) jets respectively. Since the lower speed jet is required to be shock-free (i.e. $A_{j1}/A_e = 1$) then according to Table 2.1, A_{j2}/A_{j1}=1.02. Velocity power factors $n(\theta,T_t)$ are listed in Table 2.2.

Figure 3.1 shows the actual spectral density measurements at nozzle reading of smc021-1605 in blue. In order to find the mixing noise component for this jet, we select the shock-free nozzle condition smc000-1614 as the datum jet – therefore according to Table 2.1 U_{j2}/U_{j1} = 1.04/0.91. Following equation 3.1, the mixing noise at readings smc000-1614 and smc021-1605 are designated as PSD_1 and PSD_2 respectively.

It is not surprising that the scaling law does a better job of isolating the mixing noise component at forward and sideline angles (Fig. 3.1). The aft angle spectra, as discussed in sections 2.3 and 2.4, do not collapse together when scaling consists of jets that straddle the acoustic Mach number of 1.0. Nozzle condition smc021-1605 has a fully expanded Mach number of 1.17 at $U_j/c_\infty = 1.04$, and the aft angle spectra are not expected to coalesce with scaled subsonic data (Fig. 3.1b).

Assuming that two noise components are incoherent, then the mixing noise (seen as dark line in Fig. 3.1) is subtracted from the total noise to find the shock noise

$$10^{PSD(shock)/10} = 10^{PSD(total)/10} - 10^{PSD(mixing)/10}. \qquad (3.2)$$

Fig. 3.2 displays the actual power spectral density of the shock-associated noise at nozzle conditions of smc021-1605.

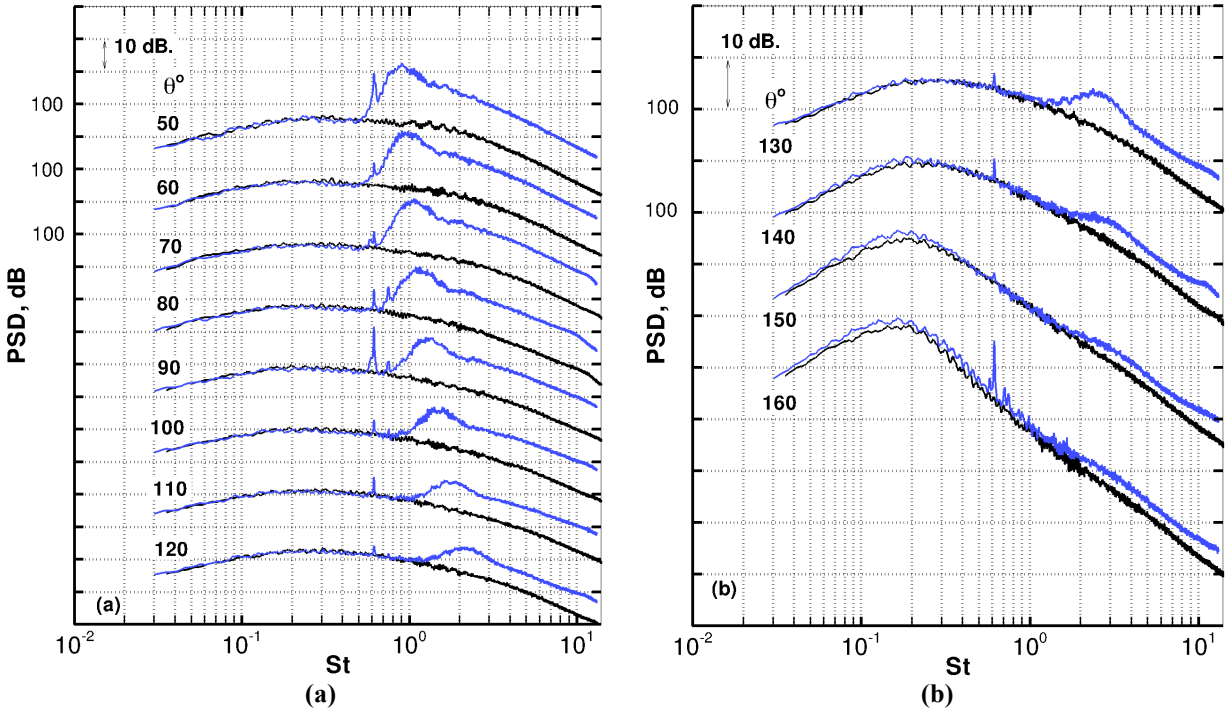

Fig. 3.1 (a) and (b) : blue line - Measured jet noise spectra in an under-expanded convergent nozzle smc021-1605 (Table 2.1);
dark line - jet mixing noise as evaluated from velocity scaling of smc000-1614.

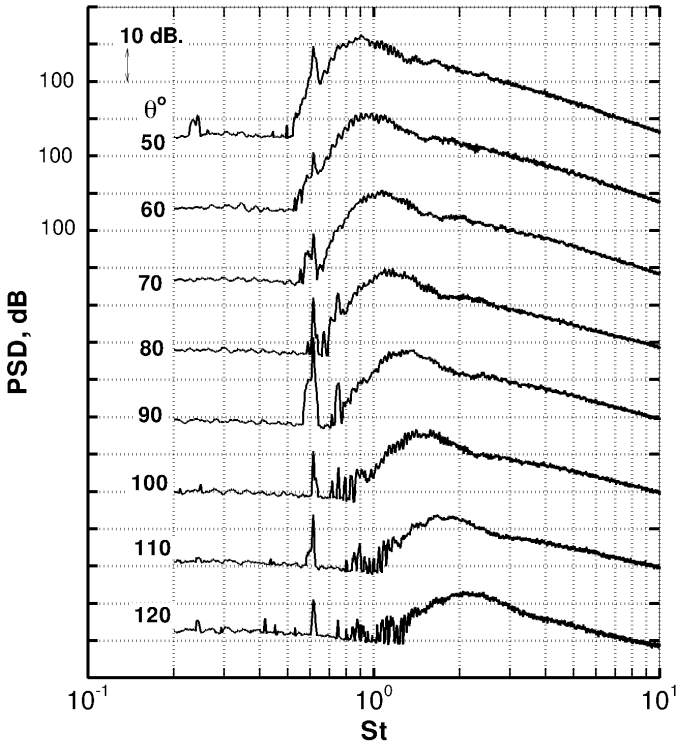

Fig. 3.2 Shock-associated noise at nozzle condition smc021-1605 (Table 2.1).

Shock-associated noise is believed to arise from the interaction of large turbulence structures with the Fourier modes of the shock cells [Ref. 23]. The primary peak frequency gets larger with increasing the inlet angle θ. According to Fig. 3.2, much weaker peaks also follow the primary peak frequency of the broadband shock power spectral density. The maximum PSD amplitude declines as we approach aft angles. Shock noise intensity curves in Fig. 3.2 show peak amplitudes of 112.5dB at St = 0.90, θ=50°; and 103.3dB at St = 2.2, θ=120°.

The shock-noise intensity (i.e. integrated spectrum) usually scales as β^m, where $\beta = \sqrt{M_j^2 - M_d^2}$ is the shock intensity parameter and m is the shock exponent factor. A nominal value for m is 4. Experimental measurements [Ref. 24] show that m varies with both angle and temperature and approaches 4.0 in the very forward angle where shock noise is at its peak. The least squares method described in section 1.3 is readily extended to the shock–associated noise when sufficient data is available to make the regression a success. In that case, the independent variable would have to be defined as $10Log\beta$.

Within the second category, we consider an under-expanded convergent nozzle with screech and noise amplification (such as smc000-1616 at NPR= 2.556 – Table 2.1). According to Figs. 2.1 and 2.2 strong screech tones amplify the jet mixing noise and cause the velocity power law to fail at all angles. As in the previous example, mixing noise is evaluated when we apply the velocity power law to configuration smc000-1614, and scale that up to the fully expanded jet velocity at smc000-1616. Figure 3.3 shows the measured spectra (i.e. total noise at reading 1616) in blue, and the mixing noise for this jet in dark. Due to the presence of the broadband jet noise amplification (AMN), the two curves fail to collapse together at the early stages of the spectra. The shock-associated noise for this jet is evaluated according to Eq. 3.2 (see Fig. 3.4).

A qualitative display of the screech-related amplification is shown in Fig. 3.5. Here the AMN is evaluated as delta-dB between total and mixing noise PSD amplitudes at a nominal Strouhal frequency of 0.10, which is located prior to the primary peak frequency of shock noise.

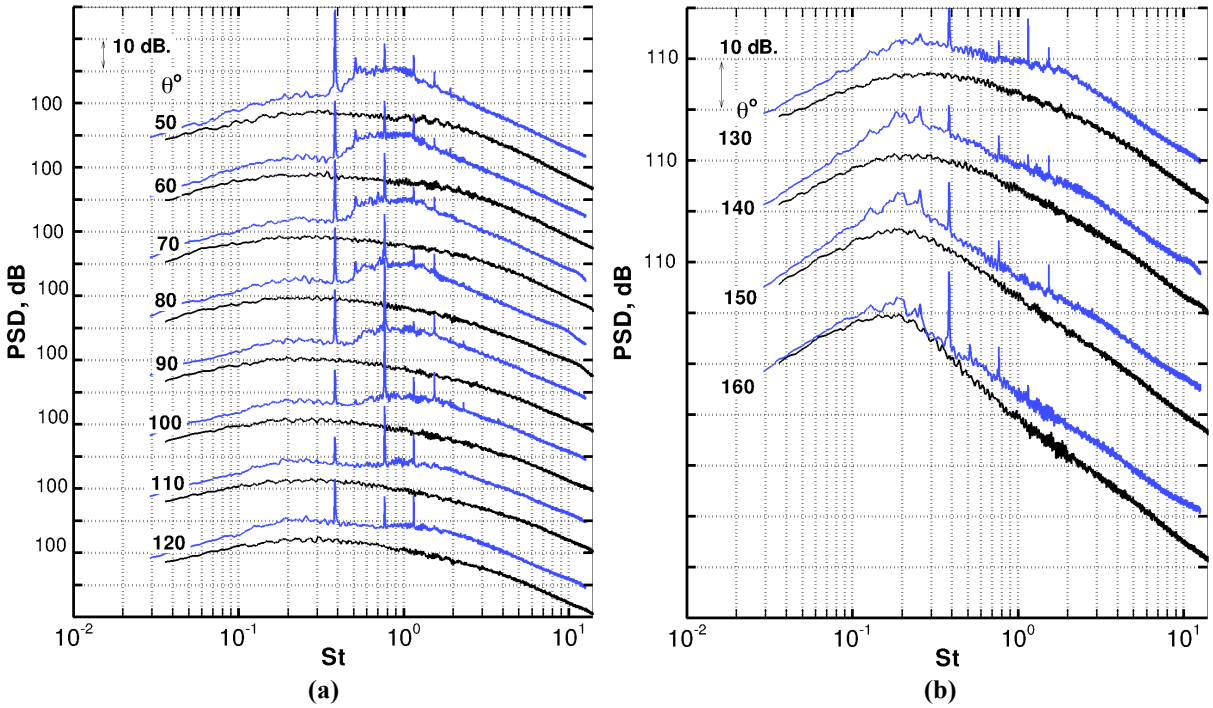

Fig. 3.3 (a) and (b): blue line - Measured jet noise spectra in an under-expanded convergent nozzle smc000-1616(Table 2.1);
dark line - jet mixing noise as evaluated from velocity scaling of smc000-1614.

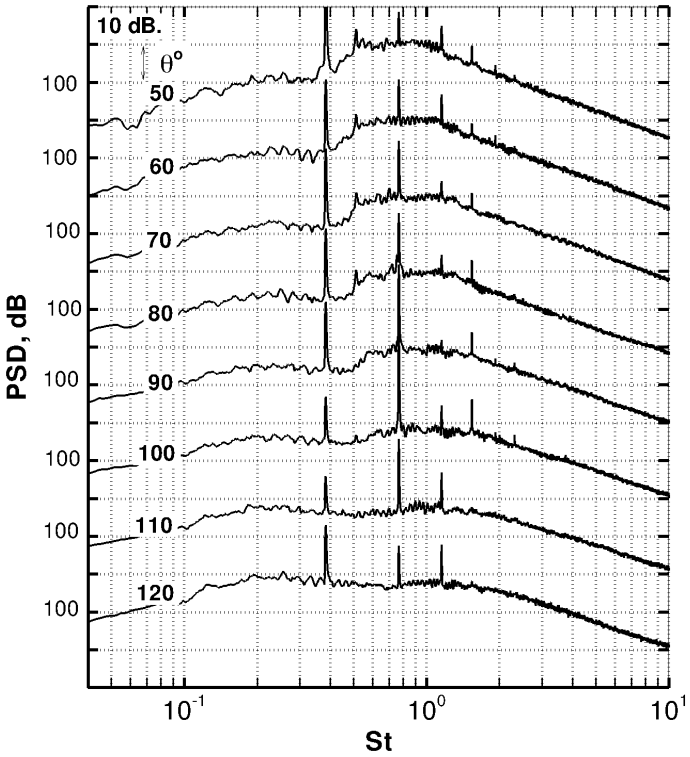

Fig. 3.4 Shock-associated noise at nozzle condition smc000-1616 (Table 2.1).

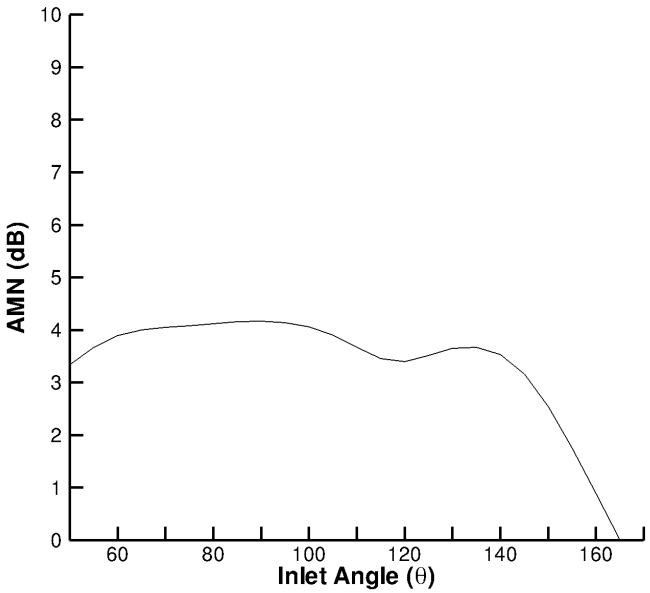

Fig. 3.5 Amplification amplitude of broadband jet noise due to screech at *St* = 0.10 in Fig. 3.3.

As an additional example within the second category of nozzles, consider an under-expanded convergent nozzle at configuration smc000-1618 in Table 2.1. Figure 3.6 shows that at a pressure ratio of 3.514 the discrepancy between spectral measurements at this set point and velocity-scaled subsonic data grow larger as we approach aft angles (also compare Figs. 3.3b and 3.6b). Unlike the previous example, this difference is not entirely screech-related. Earlier discussions of section 2 demonstrated that even in the absence of the screech, aft angle spectra fail to collapse together when the velocity power law is applied to a mix of subsonic and supersonic jets (see Fig. 2.4b). We also demonstrated that velocity power laws are successful across all jet velocities when angle θ is not close to the downstream jet axis (see Figs 2.1 and 2.2). Subsequently, the shock-associated noise for this nozzle (see Fig. 3.7) is evaluated at forward- and sideline angles when we use equation 3.2 in conjunction with the spectral elements of Fig. 3.6a.

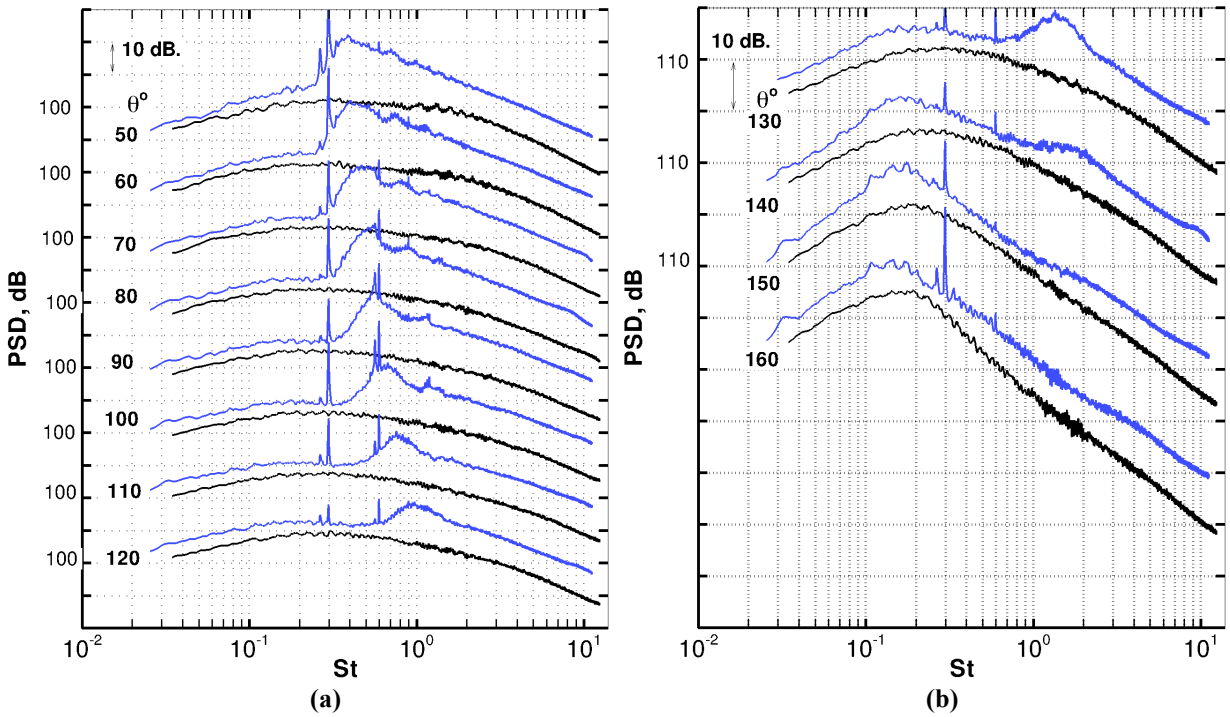

Fig. 3.6 (a) and (b): blue line - Measured jet noise spectra in an under-expanded convergent nozzle smc000-1618 (Table 2.1);
dark line - jet mixing noise as evaluated from velocity scaling of smc000-1614.

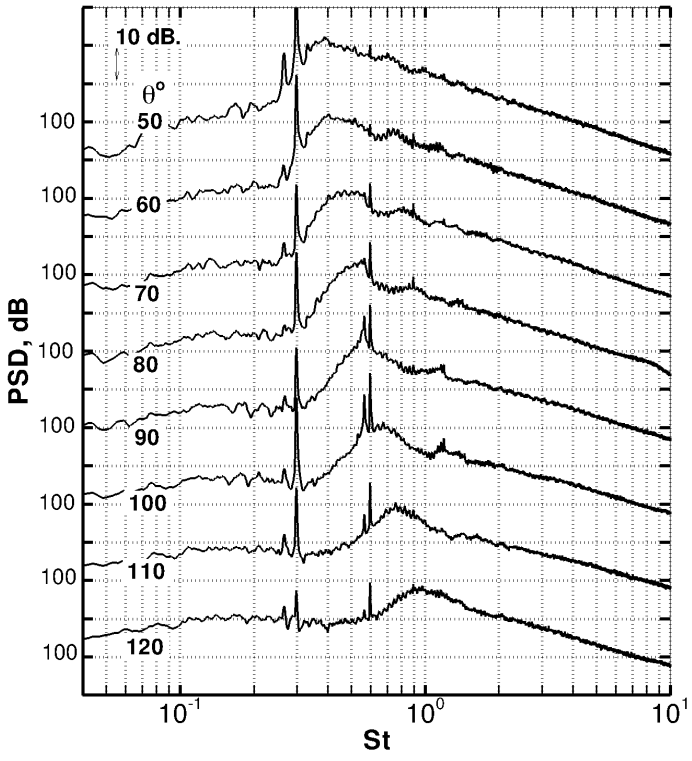

Fig. 3.7 Shock-associated noise at nozzle condition smc000-1618 (Table 2.1).

To address the third and final category of nozzles, let's consider a convergent-divergent nozzle such as smc016 at the design Mach number of 1.50. Earlier, we observed when this nozzle is operated at its design pressure ratio of 3.671 (i.e. reading 1636, Table 2.1) the mixing noise conforms to the velocity power law. We also noted a slight amount of shock-associated in the spectra (Figs. 2.1b, and 2.2).

The nozzle is now studied at highly under-expanded conditions shown in Table 3.1. At a nozzle pressure ratio of 5.99 further flow expansion to a fully expanded Mach number of 1.827 occurs outside the jet exit. As usual, the mixing noise is evaluated when we apply the velocity scaling to the mixing noise at configuration smc000-1614 (Table 2.1). Following Eq. 3.1, the mixing noise in these two jets are related through $U_{j2}/U_{j1} = 1.418/0.91$ and $A_{j2}/A_{j1} = 1.248$. The shock-associated noise is evaluated as before when we substitute the two noise elements of Fig. 3.8a into Eq. 3.2. Shock noise spectra in Fig 3.8b show that the primary peak Strouhal frequency for this nozzle is lower compared to the previous examples. The secondary shock-related peaks are also seen clearly following the primary peak.

Table 3.1 SHJAR readings in CD nozzle smc016

Rdg	Nozzle	T_s	T_t	U_j / c_∞	M	NPR	M_j	A_j / A_e
1644	smc016	0.602	1.0	1.418	1.50	5.99	1.827	1.248

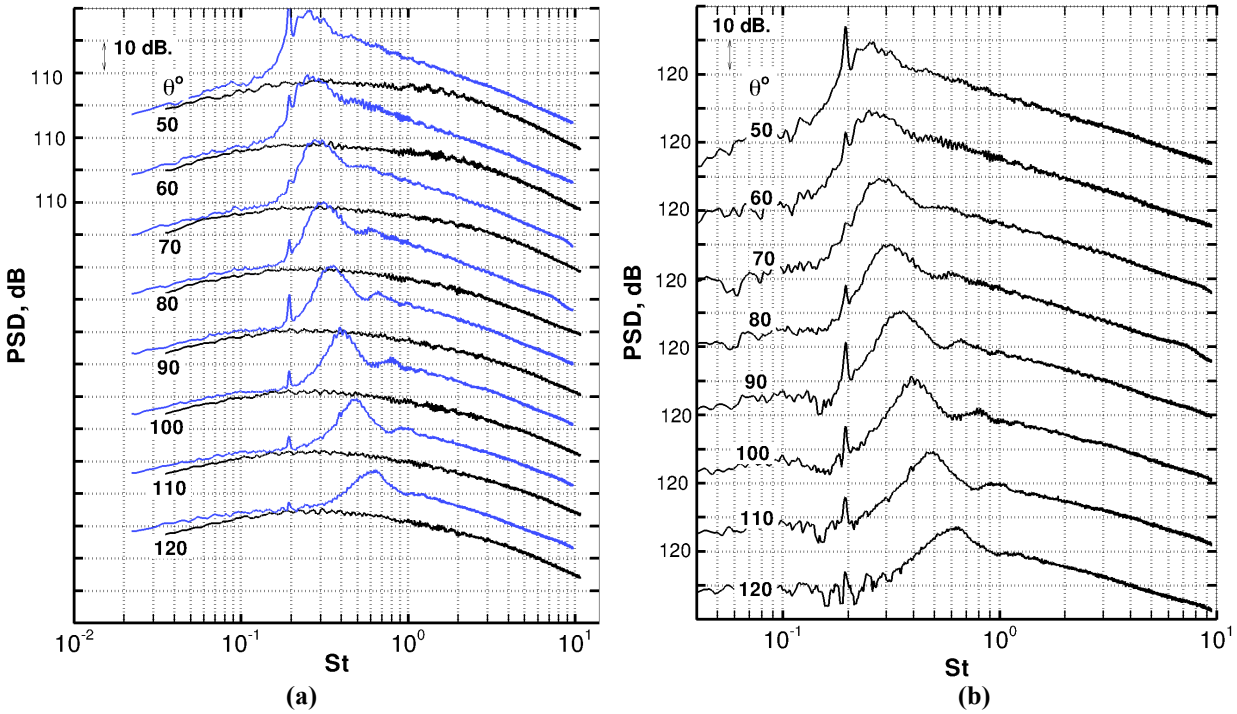

Fig. 3.8 (a): blue line - Measured jet noise spectra in an under-expanded CD nozzle smc016-1644 (Table 3.1); dark line - jet mixing noise as evaluated from velocity scaling of smc000-1614 (Table 2.1);
(b): shock-associated noise at nozzle condition smc016-1644.

3.2 Aft Angle Noise Components in Supersonic Jets

In section 2 application of the velocity power law was discussed in detail across a range of angles and temperatures. The velocity scaling of the jet mixing noise was shown as a success only when the observer angle θ is not close to the downstream jet axis. It was also demonstrated that velocity scaling at aft angles is "fairly" successful when we limit the jet acoustic Mach number to subsonic cases, and additionally choose the Helmholtz number to represent the frequency parameter. The term *fairly* highlights that even under such restrictive conditions, the *PSD* collapse occurs not throughout the spectrum, but only at a segment associated with the high-frequency roll-off of the jet noise spectra. The low frequency amplitudes continue to weaken gradually, and approach a limit level at an acoustic Mach number of 1.0.

When supersonic jets are also included in the velocity scaling, the forward and sideline spectral collapse remain unaffected (apart from the shock-associated noise), however a departure in the high frequency roll-off is noticed at aft angles and at supersonic speeds. The low frequency amplitudes, in the meantime, near a limit level (see Figs. 2.4, 2.9, 2.10).

These observations suggest that a second noise component complements the mixing noise at aft angles, and it becomes exceedingly more efficient with jet velocity. If we suppose that the first noise component PSD_1 follows velocity scaling per Helmholtz number, then supersonic jet noise spectra at aft angles could be considered as a superposition of two incoherent components if the 2nd component is viewed as a departure from velocity-scaled subsonic data.

$$10^{PSD_2/10} = 10^{Total/10} - 10^{PSD_1/10} \tag{3.3}$$

Unlike the sideline spectra discussed in section 3.1, a digression from scaled subsonic spectra at aft angles is not entirely linked to shock noise. Aft angle data presented in section 2 demonstrated that a second component is present even when jets are completely shock-free.

In general, attempts to split the power spectral density of supersonic jets into components is less successful when shock noise and its attributes, such as screech and amplification, are also present at aft angles. In such cases, it might be very difficult to completely decouple the mixing noise from the shock-associated noise.

As an example consider convergent nozzle smc000 at supersonic condition 1618 (see Table 2.1). Sample velocity-scaled spectra for this nozzle were shown earlier (Figs. 2.2 and 2.4) when the power law was examined at stagnation temperature 1.0. The 150^o spectrum, as seen in Figs. 2.3b and 2.4b, may be viewed as a superposition of two components if the second component is recognized as a departure from a velocity scaled subsonic spectra at a condition such as smc000-1614.

Figures 3.9a shows the measured power spectral density per Strouhal frequency at subsonic condition 1614 (jet 1), as well as supersonic condition 1618 (jet 2) at 150^o. Fig. 3.9b shows the PSD for the same two jets but per Helmholtz frequency after adjustments of -10Log(0.91) and -10Log(1.23) in the respective levels of Fig. 3.9a. Note that a relative vertical shift of $10Log(1.23/0.91)$ takes place between the two spectra. In the next step, the power level at condition 1614 is scaled to the jet velocity at reading 1618 using n= 9.13 (Table 2.2) combined with the power law Eq. 3.1. The gap between the two spectra is additionally reduced by

$$10(9.13)\,Log(1.23/0.91) + 10Log(1.156)\,.$$

The velocity scaled subsonic spectra (denoted as PSD_1) is now considered as the 1st component in the power density of the supersonic jet (shown as green line in Fig. 3.9c). Note that steps b and c, effectively

increment the velocity power factor from n to n+1. Finally, the second spectral component PSD_2 as evaluated per Eq. 3.3 is shown in Figure 3.9d. In this example, slight contributions from shock-associated noise are also coupled with the 2nd noise component as seen in the latter part of the spectrum.

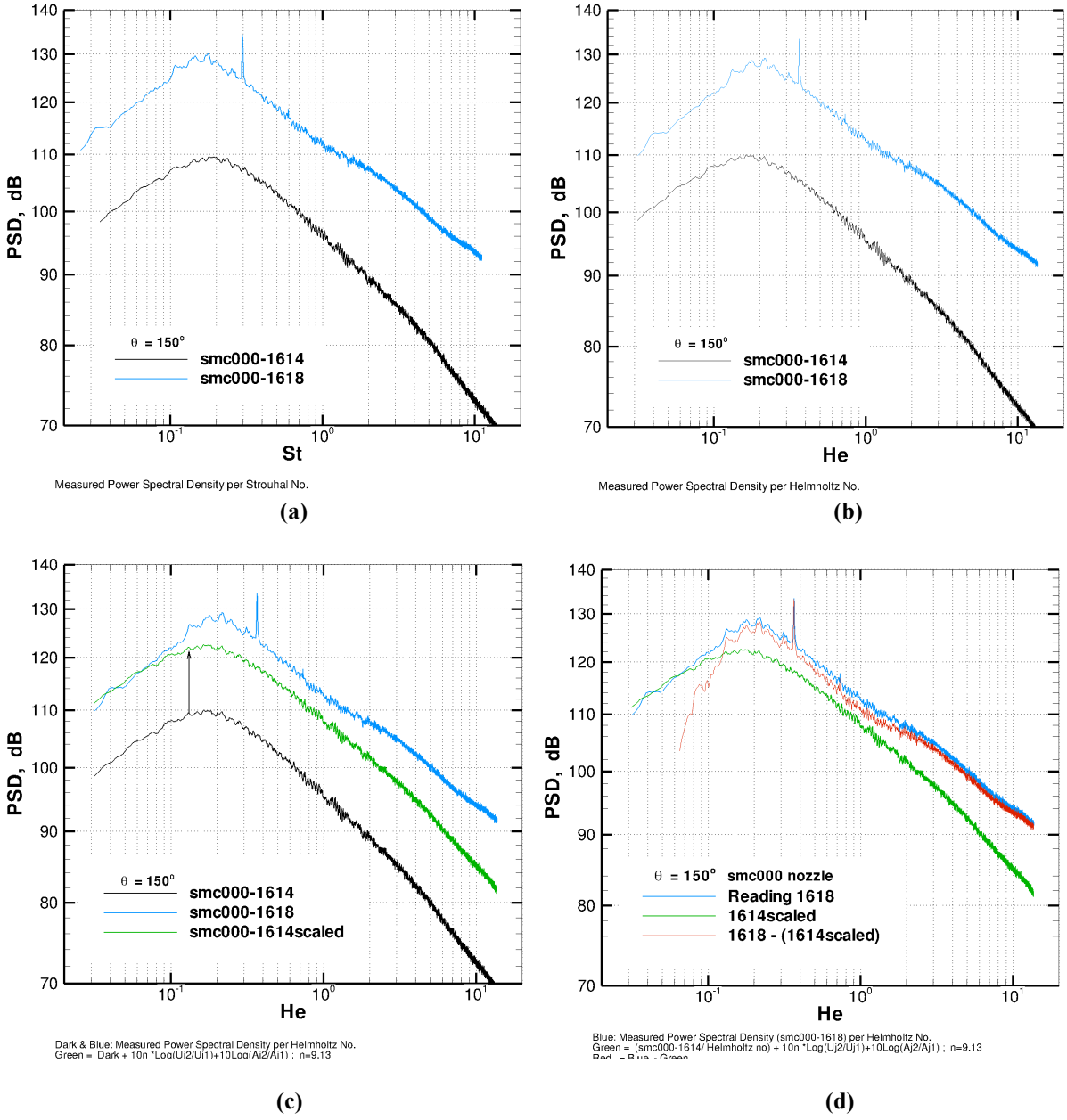

Fig. 3.9 (a) Measured PSD per Strouhal number: 1618 (blue); 1614 (dark)
(b) Measured PSD per Helmholtz number: 1618 (blue); 1614 (dark).
(c) PSD per Helmholtz number scaled from 1614 (dark) to 1618 (green) with n=9.13;
(d) PSD at condition 1618 split into two components (red and green).

Summary

An extensive database of single flow jet noise data has been analyzed, keying on correlating power spectral density as a function of angle over different temperatures and velocities. A common spectral directivity with velocity scaling has been established at each temperature, and competing noise sources has been separated from acoustic spectra. Examination of various spectral figures shows that:

- Velocity scaling laws are equally successful at constant static or stagnation temperature, and are implemented using velocity power factor n as long as temperature is held constant. Application of the power law across jets of different temperatures requires two parameters n and B.
- Spectral collapse of the jet mixing noise power spectral density with Strouhal frequency is achieved successfully at forward and sideline angles at all frequencies and Mach numbers.
- The spectral shape at small aft angles changes across the acoustic Mach number of 1.0.
- At small aft angles, a collapse of the high frequency roll-off of amplitudes is achieved with Helmholtz frequency when the acoustic Mach number is subsonic.
- Amplification of the jet mixing noise in the presence of screech is identified with the aid of the scaling laws.
- Shock-related noise may be subtracted from the total spectrum when the scaling laws are used to identify the jet mixing noise.
- Supersonic jet noise spectra at small aft angles may be divided into two incoherent components if the second component is viewed as a departure from the scaled-up subsonic spectra.

The interpretation of the scaling laws into noise generation mechanisms and jet noise prediction models should follow this analysis.

References

[1] Lighthill, M. J., "On Sound Generated Aerodynamically: 1. General Theory," Proceedings of the Royal Soc. (London), **211A**, pp. 564-587, 1952.
[2] Goldstein, M. E., *Aeroacoustics*, McGraw Hill, 1976
[3] Viswanathan, K., "Scaling Laws and a Method for Identifying Components of Jet Noise," *AIAA Journal*, **44(10)**, pp. 2272-2285, 2006.
[4] Tam, C. K. W., "Dimensional Analysis of Jet-Noise Data," *AIAA Journal*, **44(3)**, pp. 512-522, 2006.
[5] Bechert, D. and Pfizenmaier, E., " On the Amplification of Broadband Jet Noise by Pure Tone Excitation," *J. Sound and Vibration*, **43**, 1975, pp. 581-587.
[6] Ahuja, K. K. and Blankney, D. F., "Tone Excited Jets, Part IV: Acoustic Measurements," *J. Sound and Vibration*, **102(1)**, 1985, pp. 93-118.
[7] Moore, C. J., " The Role of Shear-Layer Instability Waves in Jet Exhaust Noise," *J. Fluid Mechanics*, **80**, 1977, pp. 321-367.
[8] Bridges, J. and Brown, C. A., "Validation of the Small Hot Jet Rig for Jet Noise Research", AIAA Paper 2005-2846, May 2005.
[9] Brown, C. A., and Bridges, J., "Small Hot Jet Acoustic Rig Validation," NASA TM – 2006-214234, 2006.
[10] Bridges, J., and Wernet, M. P. "Measurements of the Aeroacoustic Sound Sources in Hot Jets," AIAA Paper 2003-3130, 2003.
[11] Bridges, J., and Wernet, M. P. "Effect of Temperature on Jet Velocity Spectra," AIAA Paper 2007-3628, 2007.
[12] Lush, P. A., "Measurements of Subsonic Jet Noise and Comparison with Theory," *J. Fluid Mechanics*, **46(3)**, pp. 477-500, 1971.
[13] Hoch, R. G., Duponchel, J. P., Cockling, B. J., and Bryce, W. D., "Studies of the Influence of Density on Jet Noise," *J. Sound and Vibration*, **28(4)**, pp. 649-668, 1973.
[14] Ahuja, K. K., and Bushell, K. W., "An Experimental Study of Subsonic Jet Noise and Comparison with Theory," *J. Sound and Vibration*, **30(3)**, pp. 317-341, 1973.
[15] Tanna, H. K., "An Experimental Study of Jet Noise, Part I: Turbulent Mixing Noise." *J. Sound and Vibration*, **50(3)**, pp. 405-428, 1977.
[16] Tanna, H. K., "An Experimental Study of Jet Noise, Part II: Shock Associated Noise." *J. Sound and Vibration*, **50(3)**, pp. 429-444, 1977.
[17] Bates, D. M., and Watts, D. G., *Nonlinear Regression Analysis and its Applications*, John Wiley & Sons, 1988.
[18] Viswanathan, K., "Aeroacoustics of Hot Jets," *J. Fluid Mechanics*, **516**, pp. 39-82, 2004.
[19] Seiner, J. M., and Norum, T. D., "Experiments on Shock Associated Noise of Supersonic Jets," AIAA Paper 79-1526,1979.
[20] Seiner, J. M., and Norum, T. D., "Aerodynamic Aspects of Shock Containing Jet Plumes," AIAA Paper 80-0965, 1980.
[21] Norum, T. D., and Seiner, J. M., "Measurements of Mean Static Pressure and Far Field Acoustics of Shock-Containing Supersonic Jets," NASA TM–84521, 1982.
[22] Harper-Bourne, M., and Fisher, M. J., "The Noise from Shockwaves in Supersonic Jets," Proceedings (No. 131) of the AGARD Conference on Noise Mechanisms, Brussels, Belgium, 1973.
[23] Tam, C. K. W., and Tanna, H. K., "Shock Associated Noise of Supersonic Jets from Convergent-Divergent Nozzles," *J. Sound and Vibration*, **81(3)**, pp. 337-358, 1982.
[24] Viswanathan, K., Alkislar, M., and Czech, M., "Characteristics of the Shock Noise Component of Jet Noise," AIAA Paper 2008-2835, 2008.

REPORT DOCUMENTATION PAGE	Form Approved OMB No. 0704-0188

1. REPORT DATE *(DD-MM-YYYY)*	2. REPORT TYPE	3. DATES COVERED *(From - To)*
01-03-2009	Technical Memorandum	

4. TITLE AND SUBTITLE
SHJAR Jet Noise Data and Power Spectral Laws

5a. CONTRACT NUMBER
NNC06BA07B

5b. GRANT NUMBER

5c. PROGRAM ELEMENT NUMBER

6. AUTHOR(S)
Khavaran, Abbas; Bridges, James

5d. PROJECT NUMBER

5e. TASK NUMBER

5f. WORK UNIT NUMBER
WBS 561581.02.08.03.18.03

7. PERFORMING ORGANIZATION NAME(S) AND ADDRESS(ES)
National Aeronautics and Space Administration
John H. Glenn Research Center at Lewis Field
Cleveland, Ohio 44135-3191

8. PERFORMING ORGANIZATION REPORT NUMBER
E-16923

9. SPONSORING/MONITORING AGENCY NAME(S) AND ADDRESS(ES)
National Aeronautics and Space Administration
Washington, DC 20546-0001

10. SPONSORING/MONITORS ACRONYM(S)
NASA

11. SPONSORING/MONITORING REPORT NUMBER
NASA/TM-2009-215608

12. DISTRIBUTION/AVAILABILITY STATEMENT
Unclassified-Unlimited
Subject Categories: 01 and 71
Available electronically at http://gltrs.grc.nasa.gov
This publication is available from the NASA Center for AeroSpace Information, 301-621-0390

13. SUPPLEMENTARY NOTES

14. ABSTRACT
High quality jet noise spectral data measured at the Aeroacoustic Propulsion Laboratory at the NASA Glenn Research Center is used to examine a number of jet noise scaling laws. Configurations considered in the present study consist of convergent and convergent-divergent axisymmetric nozzles. The measured spectral data are shown in narrow band and cover 8193 equally spaced points in a typical Strouhal number range of 0.0 to 10.0. The measured data are reported as lossless (i.e., atmospheric attenuation is added to measurements), and at 24 equally spaced angles (50° to 165°) on a 100-diameter (200-in.) arc. Following the work of Viswanathan, velocity power factors are evaluated using a least squares fit on spectral power density as a function of jet temperature and observer angle. The goodness of the fit and the confidence margins for the two regression parameters are studied at each angle, and alternative relationships are proposed to improve the spectral collapse when certain conditions are met. As an immediate application of the velocity power laws, spectral density in shock-containing jets are decomposed into components attributed to jet mixing noise and shock noise. From this analysis, jet noise prediction tools can be developed with different spectral components derived from different physics.

15. SUBJECT TERMS
Jet aircraft noise; Propulsion noise; Flow noise; Noise

16. SECURITY CLASSIFICATION OF:			17. LIMITATION OF ABSTRACT	18. NUMBER OF PAGES	19a. NAME OF RESPONSIBLE PERSON
a. REPORT	b. ABSTRACT	c. THIS PAGE			STI Help Desk (email:help@sti.nasa.gov)
U	U	U	UU	62	19b. TELEPHONE NUMBER *(include area code)* 301-621-0390